

Project information

Project full title	Connecting Russian and European Measures for Large-scale Research Infrastructures – plus
Project acronym	CREMLINplus
Grant agreement no.	871072
Instrument	Research and Innovation Action (RIA)
Duration	01/02/2020 – 31/01/2024
Website	www.cremlinplus.eu

Deliverable information

Deliverable no.	D5.3 (D46)
Deliverable title	Status report on R&D work on central tracker for the SCT detector
Deliverable responsible	INFN
Related Work-Package/Task	WP5; Task 5.5
Type (e.g. Report; other)	Report
Author(s)	
Dissemination level	Public
Document Version	
Date	
Download page	https://www.cremlinplus.eu/results/deliverables/

Document information

Version no.	Date	Author(s)	Comment
1.0	11.01.2022	Francesco Grancagnolo, Alexandr Popov, Vyacheslav Ivanov	



Table of Contents

1. Introduction.....	3
2. The mechanics of the SCT drift chamber prototype (CMD-3).....	4
2.1 Introduction.....	4
2.2 Layout of the CMD-3 drift chamber	4
2.3 The “wire cage”	7
2.4 Preliminary Finite Element Analysis (FEA).....	9
3. The BINP Magnetron for wire coating.....	11
4. Development of a fast digitizer-FPGA board for cluster counting	15
5. The beam test for cluster counting	17
5.1 Introduction.....	17
5.2 Garfield++ simulation of ionization clustering	17
5.3 Evaluation of the simulation algorithm.....	19
5.4 Geant4 simulation of ionization clustering	20
5.5 Discrepancy between Garfield++ and Geant4 results.....	21
5.6 Motivation for a beam test	22
5.7 The test setup.....	22
5.8 Preliminary results on gas gain.....	26
5.9 Preliminary results on space charge.....	27
5.10 Preliminary results on cluster counting algorithms	29
6. Simulation of the SCTF drift chamber	30
6.1 Generation of the DC geometry	30
6.2 Simulation of the particles passage through the DC material.....	31
6.3 Simulation of the digitized signals from the wires	32
6.4 Hit reconstruction.....	33
6.4.1. Peaks merging and z–coordinate reconstruction.....	33
6.4.2. Peaks clusterization	34
6.4.3. Reconstruction of track impact parameter	35
6.5 Track finding	35
6.6 Track fitting.....	35
6.7 Particle identification	37
7. Prospects and conclusions.....	39



1. Introduction

The aim of task 5.5 is to foster efforts of the international community on R&D around the central tracker of the SCT detector.

TraPId (Tracking and Particle Identification), the Central Tracker proposed by the Bari and Lecce INFN groups for the detector at SCT is an ultra-light drift chamber equipped with cluster counting/timing readout techniques. Main peculiarities of this design are the high transparency in terms of multiple scattering contributions to the momentum measurement of charged particles and the very promising particle identification capabilities.

TraPId is a down sized drift chamber from a larger one designed for the IDEA detector at both FCC-ee and CEPC, the proposed future circular e+e- colliders. It is inspired by the original design of the KLOE drift Chamber, successfully operated at the Daphne facility of the Frascati INFN Laboratories for 20 years (from 1999 until 2019) and culminated with the construction of the MEG2 drift chamber, which has just completed the commissioning phase at the PSI laboratories in Zurich and is ready to start data taking in 2022.

A drift chamber prototype for TraPId (to be used as the central drift chamber of the CMD-3 experiment at VEPP-200) is going to be developed and tested by groups from INFN Lecce, INFN Bari and BINP.

The TraPId R&D program developed over the last two years has regarded five different topics.

1. Mechanical design of the drift chamber end plates with a novel tension recovery scheme to minimize the amount of material in front of the end-plate crystal calorimeter.
2. Development of a new type of field wires based on carbon monofilaments coated with a thin metal sheet to allow for ease of soldering.
3. Development of a fast digitizer coupled to a FPGA for fast filtering and pre-analysis of the signal spectra, aiming at strongly reducing the amount of data transfer.
4. Beam test on different configurations of drift tubes to establish the optimal operating parameters for an efficient application of the cluster counting technique.
5. Simulation and reconstruction of tracks in the TraPId drift chamber exploiting the cluster counting technique for particle identification and the cluster timing technique for improving the impact parameter resolution.



2. The mechanics of the SCT drift chamber prototype (CMD-3)

2.1 Introduction

The construction of CMD3 drift chamber is driven by two main purposes:

- Maximize the transparency in terms of radiation length.
- Maximize the mechanical stability by reducing to acceptable limits the deformations of the endplates under the total load of the wires.

A significant reduction in the amount of material at the end plates is obtained by separating the gas containment function from the wire tension support function. The wires are anchored to a self-sustaining light structure ("wire-cage") surrounded by a thin skin ("gas vessel") of suitable shape to compensate for the gas differential pressure with respect to the outside. Schematically, the wire-cage is made of a set of radial spokes, constrained at their inner ends into a tiny cylinder and extended to the outer endplate rim, thus subdividing the chamber in identical sectors. The chamber layout is obtained by stacking up radially, between adjacent spokes in each sector, printed circuit boards (PCB), where the wires ends are soldered with a well-defined pitch, alternated with spacers to set the proper cell width.

In order to minimize the deformations due to the wire load, it is necessary to create a system of adjustable tie-rods that steers the wire tension to the outer end plate rim, where a rigid cylindrical carbon fiber support structure, bearing the total wire load, is attached.

In the following, the cell layout of the chamber, the mechanical design of the wire-cage and preliminary simulations about its mechanical stability will be illustrated in detail.

2.2 Layout of the CMD-3 drift chamber

The CMD-3 drift chamber layout has to fit within the dimensions of the current CMD-2 drift chamber: 484 mm length, 609 mm outer diameter and 41 mm inner diameter. Optimization of the BGO endcap calorimeter electronics might allow extending the length of the drift chamber by about 10 mm.

Figure 2.1 represents the schematic layout of the CMD-3 drift chamber, which is divided in 4 concentric super-layers *A*, *B*, *C* and *D* and 24 identical sectors. Marked with black circles, from the inner to the outer radius, the inner, the middle and the outer cylinders are indicated. The red circles mark the separations between the different super-layers.

Super-layer *A* is made of open jet-cells with wires arranged axially. Each cell defines one of the 24 sectors and includes 12 sense wires (red dots), azimuthally staggered with respect to field wires plane (black dots). The green dots represent two guard wire layers, at the two ends of the super-layer. As shown in Figure 2.2, the cell width increases from the inner to the outer radius up to the value of 28.4 mm.

The middle cylinder at 120 mm radius divides the axial super-layer *A* from the next one, so that one could insert a thin mylar foil to separate the two volumes and use two different gas mixtures, to compensate the much longer drift times of the super-layer *A*. The mechanical design is being developed including this possibility.

Super-layers *B*, *C* and *D* are made of single-wire cells with the wires arranged in an appropriate stereo angle configuration with 4 layers of 4 (5) cells per each sector *B* (*C*) and 8



layers of 6 cells per each sector D , as shown in Figure 2.3. The square cell size increases from 8.7 mm at the innermost radius to 12.4 mm at the outermost radius.

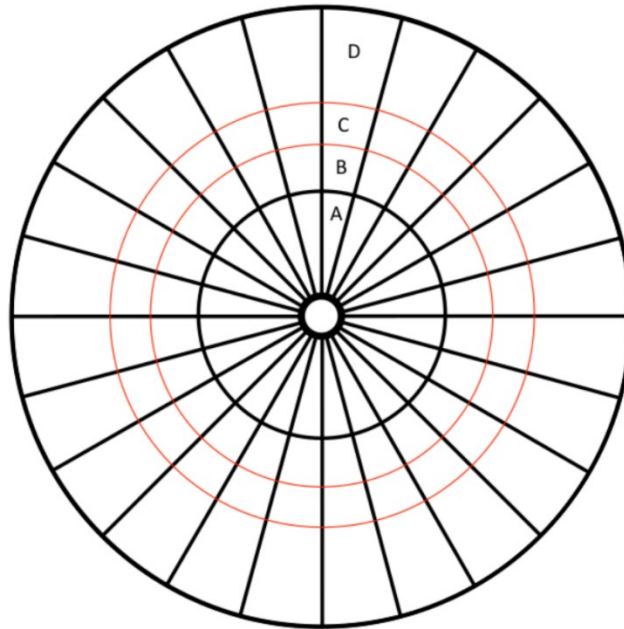


Figure 2.1. Schematic layout of the CMD-3 drift chamber

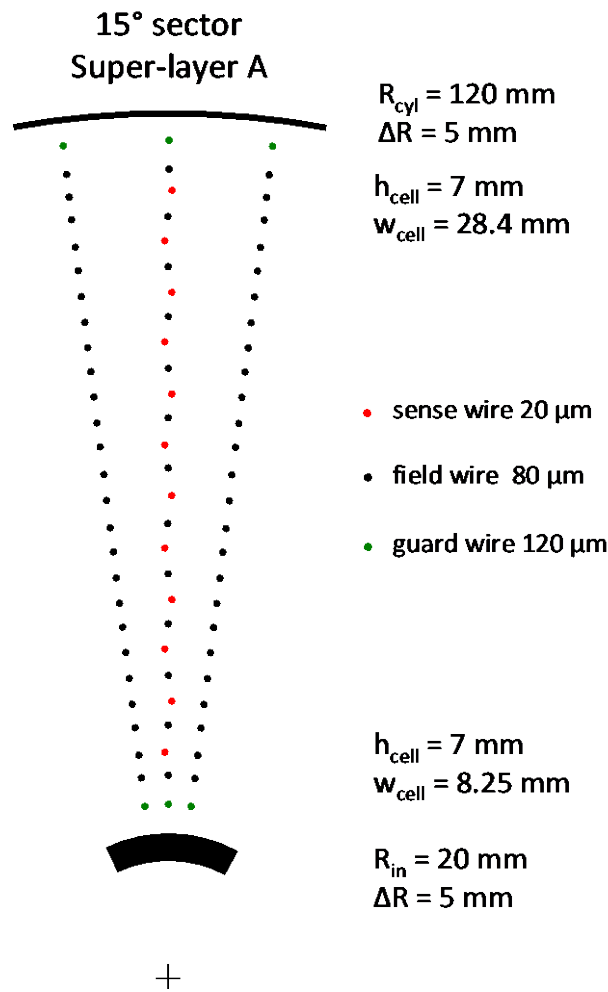


Figure 2.2. Cell structure in super-layer A: red dots represent sense wires, green dots represent guard wires and black dots represent field wires.

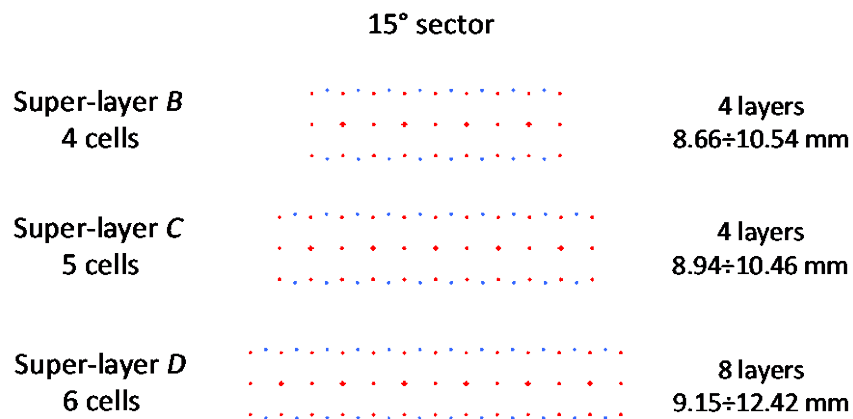


Figure 2.3. Cell layout in one layer of super-layers B, C, D. Red crosses represent sense wires, red and blue dots represent field wires. Red and blue wires are arranged at opposite stereo angles. Contiguous layers have stereo angles reversed.

The total number of drift cells (hence, sense wires) is then 2304, distributed over 28 radial layers, with a total of 12048 field and guard wires.

2.3 The “wire cage”

The structural parts of the CMD-3 drift chamber mechanics will be built in carbon fiber. Key elements of the structure: the “spokes”, the “inner ring”, the “intermediate ring”, the “outer ring” and the “outer cylinder” are illustrated in Figure 2.4.

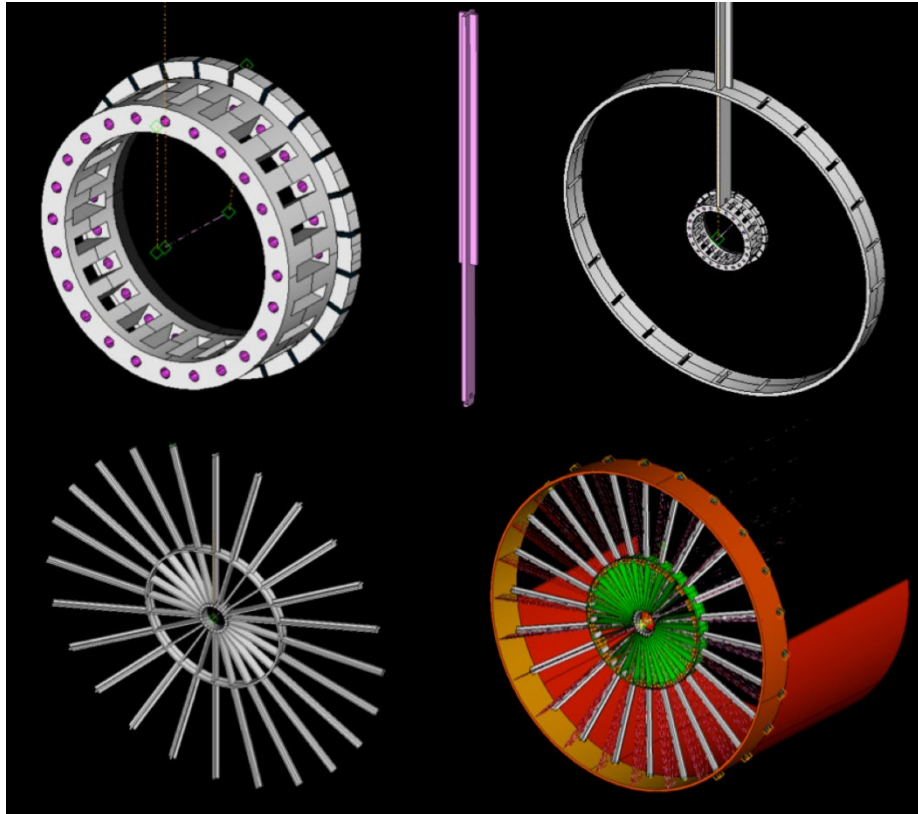


Figure 2.4. *Top left: the inner ring. Top center: the spoke. Top right: assembly of the spoke with the inner and intermediate rings. Bottom left: assembly of the 24 spokes with the inner and intermediate rings. Bottom right: the outer ring and half of the outer cylinder; the wire holding PCB’s in super-layer A and the first PCB’s of super-layer B are visible.*

The endplate assembly can be schematically summarized in the following steps.

Each spoke is inserted through a slit in the intermediate ring and is fixed with a dowel pin to the inner ring, as shown in the top right part of Figure 2.4. The operation is repeated for all 24 spokes, to form the structure shown in the bottom left part of Figure 2.4. The structural outer ring (bottom right of Figure 2.4) is then placed around the spokes, which are bolted in with a proper tension (the bolts are visible in the bottom right part of Figure 2.4). The two identical endplates are then constrained at the nominal distance by means of external adjustable supports, capable of shifting longitudinally one endplate with respect to the other one.

With the endplates moved closer than the nominal chamber length, to facilitate the wiring operations, one can start the wiring procedures, which proceeds as follows for layer A.

The wire holding PCB (two per sector, see Figure 2.5a), to which the wires are soldered, are inserted on both ends of the chamber, from inside, through the slots of the inner ring (see

Figure 2.5b) and are fixed in position with properly shaped locking blocks (Figures 2.5d and 2.5e). This complete the wiring of one sector (see Figure 2.5c) and the entire procedure is repeated for all 24 sectors to complete the wiring of layer A.

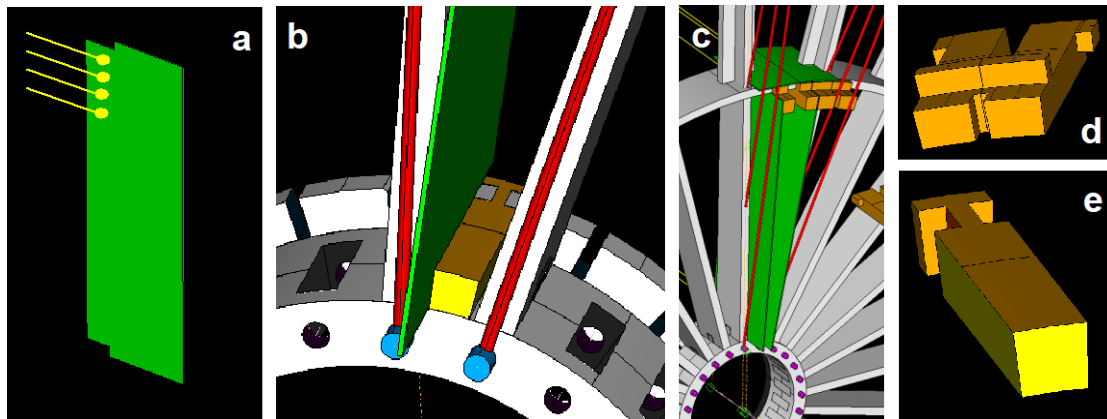


Figure 2.5. *a: the wire holding PCB; b: detail of the inner ring with the slots allowing for the passage of the wire holding PCB from the inside of the chamber and of the wedge-shaped inner locking block (e); c: one assembled sector of layer A with the two-wire holding PCB and the corresponding support blocks at the intermediate ring (d).*

Layers B, C and D are all wired in analogy to the MEG2 drift chamber. At the boundary between A and B a stereo layer of guard wires is placed to define a hyperboloid equipotential surface in order to avoid longitudinal gas gain variations for the stereo layers. As shown in Figure 2.6, the cell structure in each sub-layer is obtained by overlapping, in the order, inner field wires PCB, spacers, sense wire PCB, spacers and outer field wires PCB, all with the same stereo orientation. The spacer thickness sets the half-cell width. The stereo angle is obtained by jumping one sector from one endplate to the other. Successive sub-layers have alternating signs stereo angles.

Both spacers and wire PCB are lowered from the outer radius and are engaged around the wings of the spokes, which take the whole load from the wires mechanical tension.

In order to limit the spokes deformation, a set of stays, shown as red lines in Figures 2.5b, 2.5c and in Figure 2.6, the tension of which can be adjusted, are strung between the spokes and the structural outer ring. The whole system, shown in Figure 2.7, acts like a “harp cable stayed bridge” structure, with the outer ring acting like the tower (the pylon) and with the spoke representing the bridge deck.

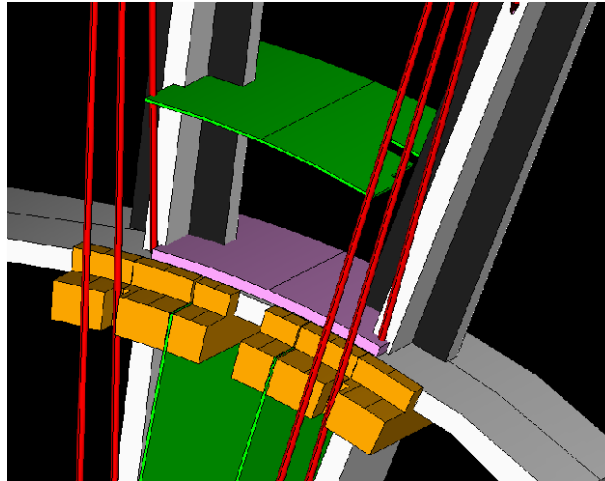


Figure 2.6. First sub-layer of layer B. The cell structure is obtained by overlapping spacers (pink) and wires PCB (green) as described in the text.

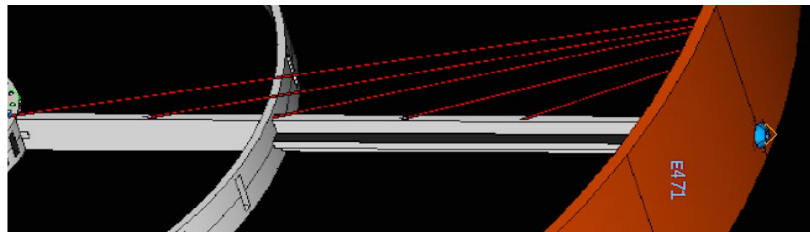


Figure 2.7. The arrangement of the system outer ring (pylon), spoke (bridge deck) and stays as in a “harp cable stayed bridge” structure.

2.4 Preliminary Finite Element Analysis (FEA)

Clearly, such an innovative concept of drift chamber endplate necessitates of the support of accurate calculations to guarantee the mechanical stability of the system. Preliminary investigations, using Finite Element Analysis, have been performed under much simpler conditions, just to establish the feasibility of the concept.

The total load due to the wire tension is of the order of 500 Kg (we assume 20 μm tungsten wires for sense, 40 and 80 μm aluminum field wires and 120 μm aluminum guard wires) or, approximately, 20 Kg per spoke. We assume a uniformly distributed load along the spoke length, with the spoke solidly constrained on one end to the non-deformable outer ring and free to flex at the other end. Using a 133 GPa low modulus carbon fiber, one gets a spoke deflection of 4.8 mm, as shown in Figure 2.8.



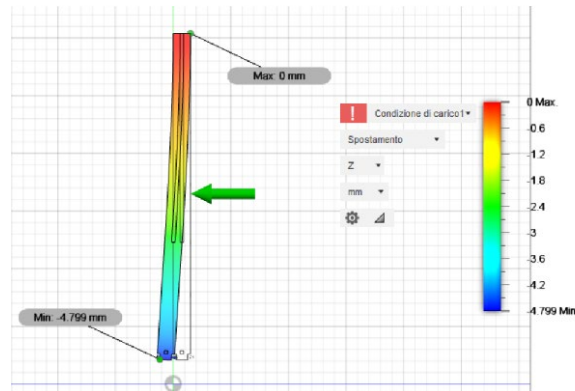


Figure 2.8. Spoke deflection under a load of 20 Kg uniformly distributed. Spoke constrained at one end and free to flex at the other end.

Just by adding the symmetry conditions of back-to-back spokes fixed to the inner ring and free of translating along the symmetry axis, the deflection is reduced to 2.2 mm, as shown in Figure 2.9a. Tensioning with 45 Kg one stay per spoke, placed at the inner ring at an angle of 10° with respect to the spoke direction, further reduces the maximum deflection to 300 μm (Figure 2.9b). Lastly, three stays per spoke, loaded with 14 Kg placed at 10° at the inner ring, 24 Kg at 14° at the intermediate ring and 20 Kg at 21° midway between the intermediate and the outer rings, reduce the maximum deflection within $\pm 25 \mu\text{m}$ (Figure 2.9c).

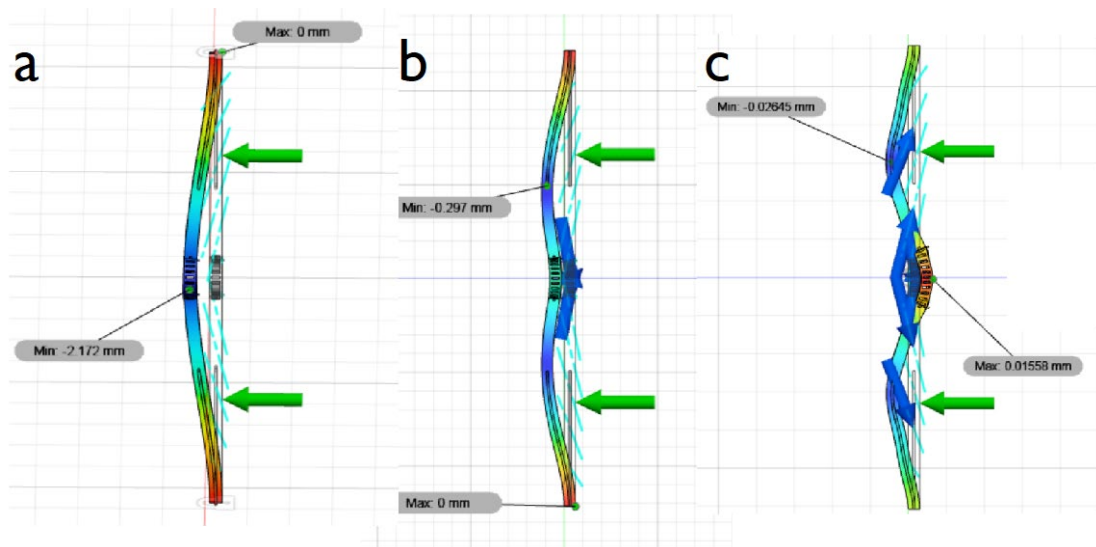


Figure 2.9. Spoke deflection under a load of 20 Kg uniformly distributed. a: symmetry condition added. b: one stay applied at the inner ring. c: three stays per spoke applied at the inner ring and at the intermediate ring and midway between the intermediate and the outer rings.

The preliminary FEA confirms that such a concept is applicable to the drift chamber of CMD-3. Obviously, a long campaign of finite elements calculations is needed to reproduce the correct constraints configurations, using the final version of the materials and shapes for the different components. Also, the reduction of the amount of material used in the endplates is the goal of the optimization of all parameters with the constraint of maximizing the stability of the entire structure.

3. The BINP Magnetron for wire coating

In the attempt of further reducing the multiple scattering contribution to the momentum measurement, a reliable technology for gold or silver coating aluminum and other metal wires and non-metallic fibers, to use them both as sense and field wires in drift chambers, has been long searched for. The problem is especially relevant for wires with a diameter of 40-50 μm , since, due to these small diameters, it is not the physical properties of the surface that matters, but the chemical resistance, which ensures the structural integrity of the wire during long-term operation. Such a small diameter does not allow for the use of electrochemistry methods for depositing metals on a surface, just as electrochemistry cannot be used for non-metallic fibers such as carbon fiber.

To this regard BINP is carrying out a research and development program on magnetron methods of sputtering on wires. Samples of 40 μm gold coated, aluminum wires and 36 μm gold coated, carbon monofilaments were obtained on the planar setup arrangement with sample lengths up to 400 mm.

The chemical resistance of the coated aluminum wire was tested as follows: coated and uncoated samples were immersed in a concentrated alkali solution, the uncoated sample completely dissolved in 200 seconds, while the coated sample reacted only through the ends.

The soldering properties of the surfaces were also tested. Figure 3.1 shows images obtained by an electron microscope of pieces of gold-coated aluminum wire (left) and gold coated carbon monofilament (right). High surface quality and good tin wettability are evident.

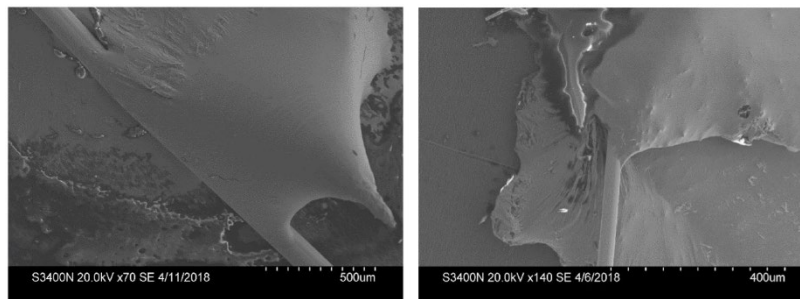


Figure 3.1. Images obtained by an electron microscope of pieces of gold-coated aluminum wire (left) and gold coated carbon monofilament (right). High surface quality and good tin wettability are evident.

The possibility of using a 0.3 μm thick copper coating on a carbon monofilament as a sense wire of a 300 mm long drift tube was tested. Its electrostatic behavior shows no differences from a tungsten sense wire. Figure 3.2 shows the comparison between a signal generated on the copper coated carbon monofilament (red pulse) and an equivalent signal generated on a 20 μm gold plated tungsten wire (blue pulse) under the same conditions. The exponential behavior of the gas gain versus the anode high voltage has also been checked.

The pilot magnetron sputtering plant built at BINP is shown in Figure 3.3. The left and right vacuum chambers contain precision mechanisms for tensioning and rewinding the wire through the discharge area.

Optimal operational parameters have been found and tests have been performed by copper coating a 125 μm diameter aluminum wire and by metallizing a 0.5 mm diameter optical fiber with a productivity of 15 m/min. Both the mechanical properties of the wire and the optical properties of the fiber did not change. Figure 3.4 shows the measured Young's modulus of the aluminum wire before and after the coating with 50 nm thickness of copper.

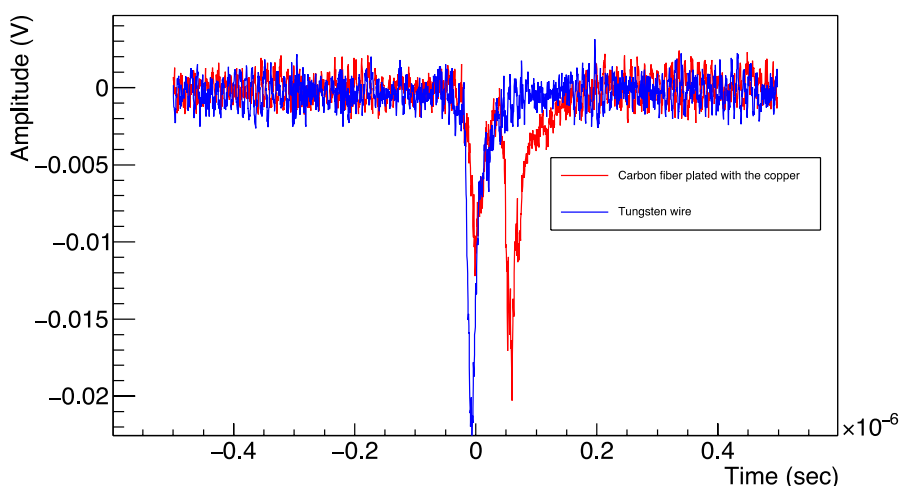


Figure 3.2. Comparison between the signal generated on the copper coated carbon monofilament (red pulse) and an equivalent signal generated on a 20 μm gold plated tungsten wire (blue pulse).

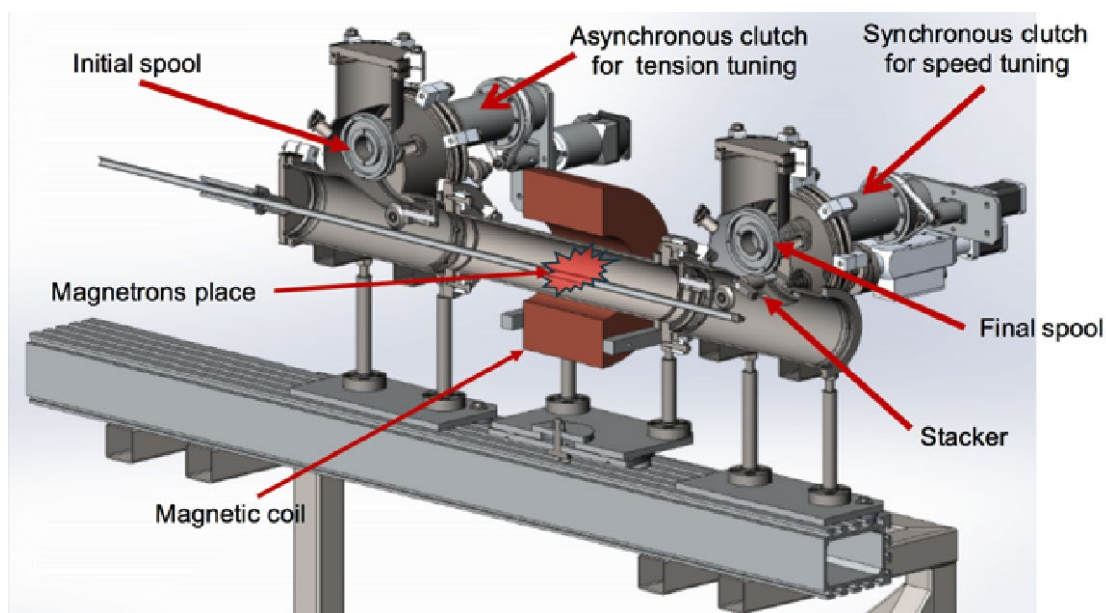


Figure 3.3. Schematic of the Magnetron sputtering facility built at BINP.

As for the thinner and less heat-dissipating 50 μm aluminum wire and for the carbon monofilament, it becomes necessary to reduce the heating in the discharge region by a factor 3.

Over the past year 2021, modifications, illustrated in Figure 3.5, have been made to the design of the magnetron, which made it possible to reduce the heating of the coated wire.

Moreover, the technology of replaceable cathodes has been developed, which allows for a relatively cheap consumption of the precious material of the sputtered cathode, while maintaining high-quality thermal contact with the cooled surface of the magnetron, thus reducing the heating of the coated wire. Figure 3.6 shows the newly produced cathodes from different materials

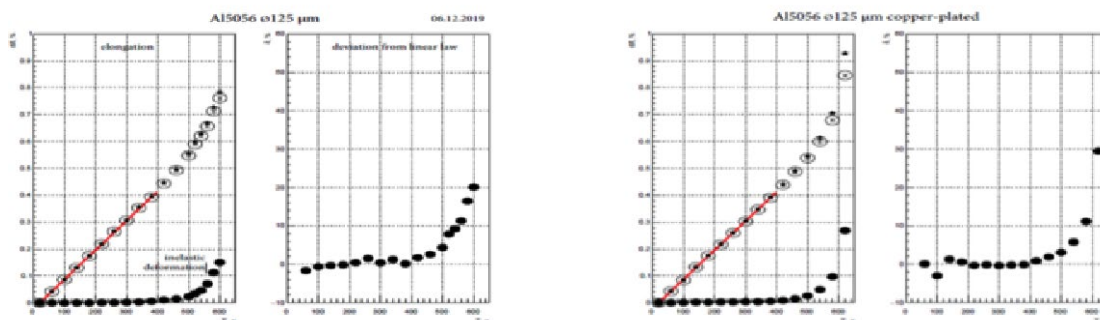


Figure 3.4. Measured Young modulus of the aluminum wire before (left) and after (right) 50 nm copper coating. No appreciable difference is measured.



Figure 3.5. Modifications implemented in 2021 on the BINP Magnetron facility.

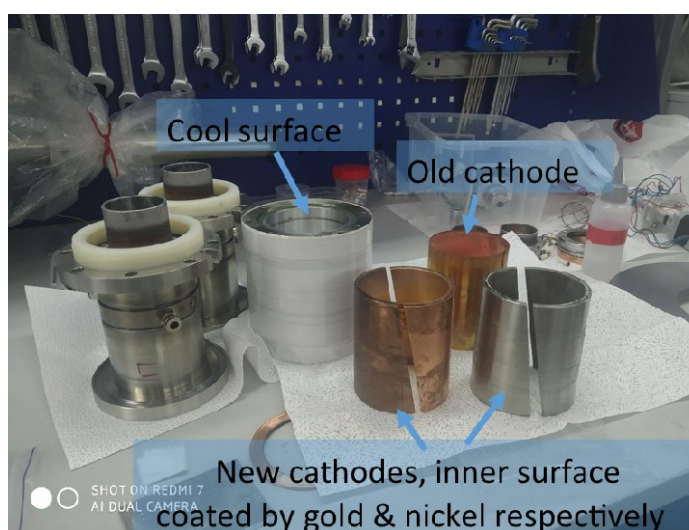


Figure 3.6. Newly produced cathodes from different materials.

For trial tests of gold and silver wire coating, a thickness of the required precious metal of up to 10 μm was applied to the working surface of the copper cathode by galvanic deposition,

which was sufficient for the tests. Figure 3.6 shows the surfaces of a 40 μm aluminum wire coated first with nickel and then gold, at various thicknesses of gold.

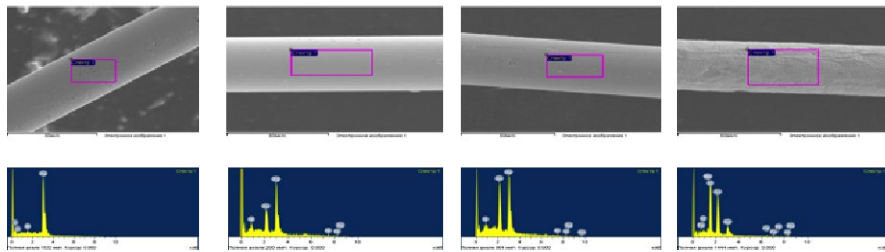


Figure 3.6. The surfaces of a 40 μm aluminum wire coated first with nickel and then gold, at various thicknesses of gold. Below, the corresponding atomic spectra of the components on the wire surface.

As shown in Figure 3.7, 10-15 nm gold is sufficient for high-quality soldering. Figure 3.8 reports the results of measuring the mechanical properties of the coated wire in comparison with the original. As it can be seen, a 10 nm layer does not modify the mechanical properties and provides high-quality soldering.



Figure 3.7. A 40 μm aluminum wire coated with 10 nm of gold. Good tin wettability and high-quality soldering are evident.

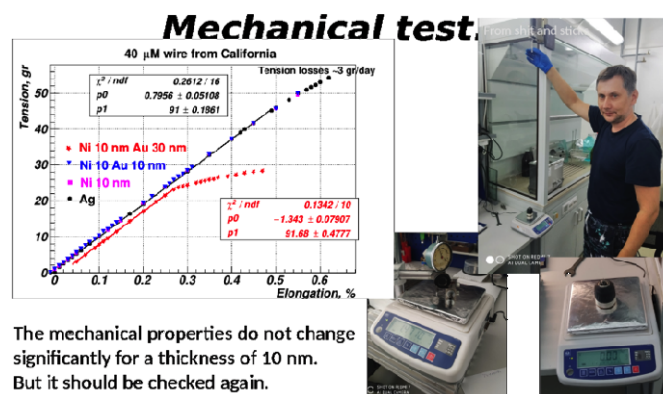


Figure 3.8. The results of measuring the mechanical properties of the coated wire in comparison with the original. As it can be seen, a 10 nm layer does not modify the mechanical properties and provides high-quality soldering.

At the moment, we have a very high consumption of the coating material, which makes the gold coating process very expensive. In the future it is planned to reduce the consumption by 3-4 times by scaling the magnetron. For the production of trial batches in the existing installation, it was decided to switch to silver, since it also provides soldering and the preserves the wire surface properties required in proportional chambers. During year 2022,



it is planned to produce a test batch of several hundred meters of 40 and 50 μm aluminum wire and of 36 μm carbon monofilament, both coated with a nickel and silver layers.

4. Development of a fast digitizer-FPGA board for cluster counting

The use of helium-based gas mixtures in the TraPId drift chamber, aimed at minimizing the multiple scattering contribution to the momentum measurement for low momentum particles, because of the low ionization cluster densities produced, introduces a sensible bias in the impact parameter reconstruction, particularly for short impact parameters and, hence, for small drift cells.

The Cluster Counting/Timing technique, which consists in measuring the arrival times on the sense wires of each individual ionization cluster, overcomes this impasse and offers the possibility of greatly improving the particle identification capabilities. However, in order to apply this technique, it is necessary to have read-out interfaces capable of processing high speed signals to efficiently isolate peaks due to different ionization clusters.

Requirements on drift chamber performance impose analog to digital conversions at sampling rates of the order of 1-2 GSa/s with at least 12-bit resolution. These constraints, together with a maximum drift time, usually of the order of several hundred ns, and with a large number of readout channels impose some sizeable data reduction, still preserving all relevant information. To this purpose, fast readout algorithms have been successfully implemented online in real time on a FPGA at a single channel level (reference: *G. Chiarello et al., "The CluTim algorithm: an improvement on the impact parameter estimates" - 2017 JINST 12 C03056*).

At the start of the processing procedure, a counter providing the timing information is activated. As the FPGA implemented algorithm identifies a peak in the real time scanning of the sense wire signal, its relative amplitude and time are stored in internal memories, which are continuously loaded as new peaks are found. At the occurrence of a trigger signal, the reading procedure is enabled and only the data related to the found peaks, in a time interval corresponding to the maximum drift time, is transferred to the external storing devices, provided it satisfies ad hoc established filtering criteria. This procedure, once applied to each readout channel, results in data reduction by factors between one and two orders of magnitude with respect to the full sampled signals.

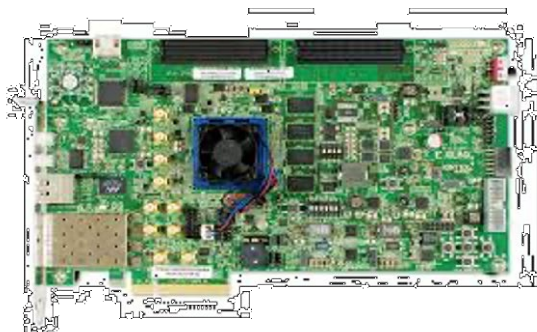
The goal of this R&D activity is to be able to implement, within a single FPGA board, more sophisticated peak finding algorithms on as many analog-to-digital conversion channels as possible, for parallel pre-processing in order to reduce costs and system complexity of the data acquisition system. Moreover, such a procedure provides, in conjunction with analogous information coming from contiguous channels, details which can be used to correlate hits to form track segments in real time, which can be used to try exploiting the possibility of defining a trigger based on track segments with latency compatible with the maximum drift time.

After the successful tests performed with a single drift channel, new and more sophisticated hardware, shown in Figure 4.1, has been acquired, to treat simultaneously two channels and to prove the feasibility of correlating contiguous hits.



The described CluTim algorithm is being improved, both in terms of counting efficiency (currently at approximately 80% level) and in terms of fake rate contaminations (at level of 1-2%).

Next step is to develop a 4-channel system and include the hits correlating algorithms to define track segments within the maximum drift time. To this purpose, collaboration with CAEN has been established within a joint project funded by the AIDAInnova program.



Xilinx Kintex UltraScale FPGA KCU105



AD9689 - 2000EBZ (dual channel)

Figure 4.1. The FPGA and the ADC for the two-channel board

A valuable alternative option is to make use of a chip developed by NALU Scientific; the ASoC chip (<https://www.naluscientific.com/technology/>) illustrated in Figure 4.2. We are expecting, within the end of January 2022, an ASoC evaluation board from Nalu Scientific and plan to complete the bench tests on the board by this summer.

Nalu Scientific is also developing a new chip: the HDSOC, with 32/64 channels, 1 GHz analog bandwidth and 2 GSa/s sampling rate. As soon as an evaluation board of this new chip will become available, we will continue exploiting this further possibility.

ASoC Eval Card

1. SMA inputs
2. ASoC chip
3. FMC for FPGA card

NALU SCIENTIFIC - 2020 IJCL NP Exchange Meeting. Copyright © 2020 Nalu Scientific LLC. All rights reserved. 11

ASoC V3 DESIGN DETAILS
Compact, high performance waveform digitizer

- High performance digitizer: 3+ CoAs
- Highly integrated
- Commercially available, low cost, patented design
- 5mm x 5mm die size

ASIC PARAMETERS	SPECIFICATION (MEASURED)
Sample rate	25 - 1.6 GSa/s
Number of channels	4
Sampling depth	16 x 16bit/channel
Signal range	0-2.5V
Resolution	10 bits/ 10b ENOB
Supply voltage	2.5V
SNR noise	~1 mV
Digital Clock frequency	28 MHz
Timing resolution	125 ps
Power die	~600 mW (1000 channels)
Alcology bandwidth	950 kHz

- Integration/Features:
 - Calibration memory on chip
 - PLL on chip
 - Isolate analog/digital voltage rings
 - Increase number of channels
 - Implement serial interface
 - Feature extraction on chip

ASoC v3
S/N: [blank]
Mfg: Q1 20 [blank]

Copyright © 2020 Nalu Scientific LLC. All rights reserved. SDR data rights may apply. 2020 DOE NP Exchange Meeting. 8

Figure 4.2. Left: The ASoC evaluation board from Nalu Scientific. Right: List of the ASoC chip parameters.



5. The beam test for cluster counting

5.1 Introduction

Particle identification is one of the crucial and difficult tasks for high energy physics experiments, like those at the future collider facilities: FCC-ee, CEPC and SCTF. The ionisation process by charged particles is the primary mechanism used for particle identification (dE/dx). However, the large uncertainties in the total energy deposition represent a limit to the particle separation capabilities. The cluster counting technique (dN/dx) takes advantage of the Poisson nature of the primary ionisation process and offers a more statistically significant method to infer the mass information.

To fully investigate the potentiality of the cluster counting techniques on real physics events, a reliable simulation of the ionisation clusters generation is needed. To this purpose, an algorithm, which uses the energy deposit information provided by the Geant4 software tools, has been developed to reproduce in a fast and convenient way the cluster size and the cluster density distributions.

The obtained results confirm that the cluster counting technique allows for reaching resolutions far better than the traditional dE/dx method (at least by a factor 2). To validate the simulations results, a first test, using a 165 GeV/c muon beam on a setup made of different size drift tubes, equipped with different diameter sense wires, has been performed at CERN by collecting data with two gas mixtures (90% He - 10% iC_4H_{10} and 80% He - 20% iC_4H_{10}) at different gas gains and at different angles between the wire direction and the ionizing tracks

The cluster counting and the cluster timing techniques, originally proposed for the drift chamber of the KLOE experiment at the DAFNE facility of INFN in Frascati (*Cataldi, G. and Grancagnolo, F. and Spagnolo, S., Cluster counting in helium-based gas mixtures, Nucl. Instrum. Meth. A 386 (1997) 458-469.*) and applied in the drift chamber of the MEG2 experiment at PSI (*A. Baldini et al., The ultra-light Drift Chamber of the MEG II experiment, Nucl. Instrum. Meth. A 958 (2020) 162152.*) will be widely exploited in the TraPid drift chamber proposed for the Super Charm-Tau Facility (SCTF).

5.2 Garfield++ simulation of ionization clustering

The process of energy loss of a charged particle crossing a medium is a discrete process: a particle traversing a gas leaves a track of ionization consisting of a sequence of clusters with one or more electrons which are all released in a single act of primary ionisation. This is a typical Poissonian process, the main advantage of which is that its Gaussian limit is achieved when the mean value reaches 20, corresponding to approximately 1 cm track length for the most commonly used gas mixtures. However, even in the most favorable momentum region (the relativistic rise region), the typical separation between energy loss curves relating to different particles is comparable to the spread around the relative mean values.

To investigate the potential of the cluster counting technique, a reasonable simulation of the ionization clusters generation is needed (*F. Cuna, N. De Filippis, F. Grancagnolo, G. Tassielli, Simulation of particle identification with the cluster counting technique, arXiv:2105.07064v1 [physics.ins-det] 14 May 2021.*).

Garfield++ (Garfield++, <https://garfieldpp.web.cern.ch/garfieldpp/>) and Geant4 (Geant4, a simulation toolkit, <https://geant4.web.cern.ch/node/1>) are two valid software tools for the



drift chamber simulations. However, Garfield++ can describe in detail the properties and the performance of a drift chamber single cell, but it is not suitable to simulate a large-scale detector and to study collider events. On the other side, Geant4 can simulate elementary particle interactions with the material of a complex detector and study collider events, but the fundamental properties and the performances of the sensible elements, like the drift cells, have to be parameterized or "ad-hoc" physics models have to be defined.

Our goal is to develop an algorithm, which can use the energy deposit information provided by Geant4, to reproduce, in a fast and convenient way, the clusters number and the cluster size distributions predicted by Garfield++.

Alternatively, one could also create a physics model, which, once integrated in Geant4, would reproduce in detail the ionization process, but this approach would imply a large disk space occupation and a long computational time. A simple algorithm using the energy deposit simulated by the software provides all the necessary information and seems to be a more suitable solution.

To this purpose, we simulated with Garfield++ tracks crossing 200 cells, 1 cm wide, filled with a mixture of 90% He - 10% iC₄H₁₀, by studying the clusters number distribution and the energy loss distribution for muons, pions, electrons, protons, and kaons in a range of momentum from 100 MeV up to 100 GeV, as reported in Figure 5.1.

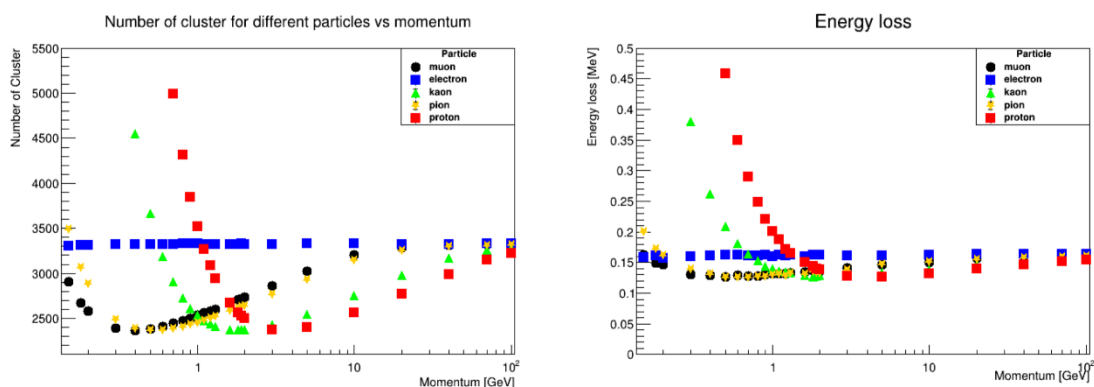


Figure 5.1. Left: Clusters number distribution. Right: Energy loss distribution.

Then we evaluated the particle separation power implementing both methods: dE/dx with a 70% truncated mean and dN/dx , as reported in Figure 5.2.

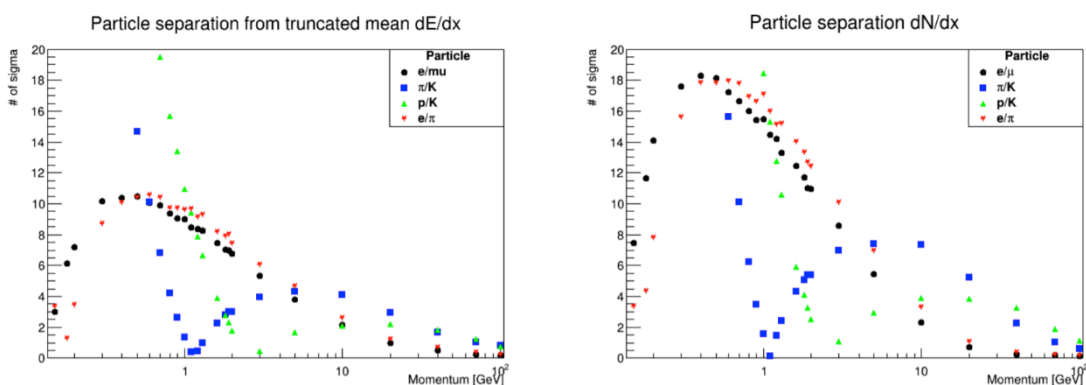


Figure 5.2. Left: Particle separation power with dE/dx (truncated mean at 70%).
Right: Particle separation power with dN/dx .

The plots show clearly that the dN/dx cluster counting technique improves particle separation capabilities by a factor of 2 with respect to the traditional dE/dx method.

Our goal is to reproduce the same result obtained with Garfield++, by using Geant4 instead. To this purpose, we implemented different algorithms to reconstruct the distributions of the number of clusters and of the cluster size, using the information provided by Geant4. Common key for all different algorithms is a model of the kinetic energy of clusters containing a single electron and of clusters containing more than one electron (see for example, Figure 5.3), built using Garfield++ simulations.

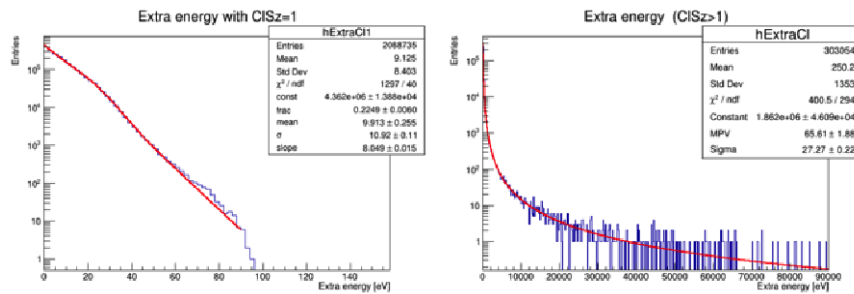


Figure 5.3. 300 MeV/c muon. Kinetic energy distribution for clusters with cluster size equal to 1 (left) and for cluster size higher than 1 (right).

Separately, the kinetic energy distribution, up to a 1 KeV, of cluster with cluster size larger than 1, a cut equivalent to the single interactions range cut set by default in Geant4, has been fitted (Figure 5.4).

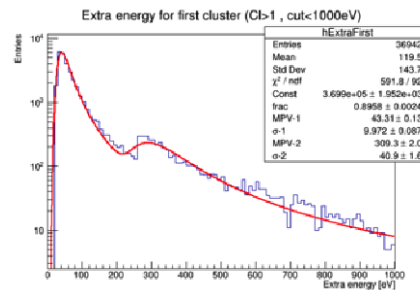


Figure 5.4. 300 MeV/c muon. Kinetic energy distribution, up to 1 KeV, for clusters with cluster size higher than 1.

The analytical functions describing the fit shown in the Figures 5.3 and 5.4 are then used in the implementation of the various algorithms.

5.3 Evaluation of the simulation algorithm

To verify the validity of the algorithms, their results are compared to the ones simulated by Garfield++, in the case of a 300 MeV/c muon with 200 hits, 1 cm wide in 90% He - 10% iC_4H_{10} gas mixture: the distribution of the number of clusters and the cluster size distribution are shown in Figure 5.5.



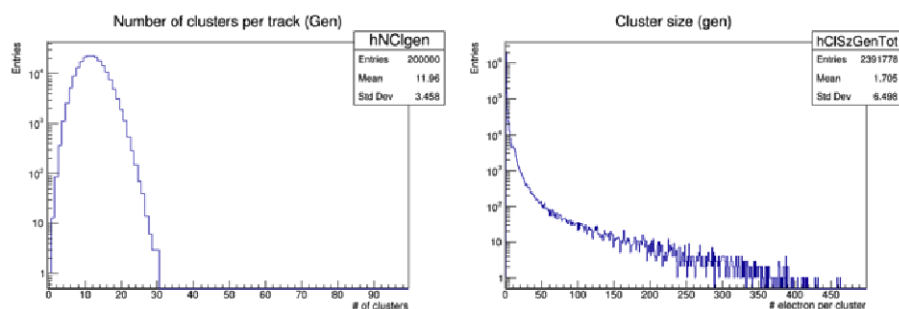


Figure 5.5. Garfield++ simulation of a 300 MeV/c muon, 200 hits, 1 cm wide.
Distributions of the number of clusters/cm (left) and of cluster size (right).

We will limit to the comparison with Garfield++ of only one of the different algorithms studied. In particular, this algorithm uses the total kinetic energy of the event to evaluate "a priori" the number of clusters, according to a likelihood criterion. Figure 5.6 shows its results.

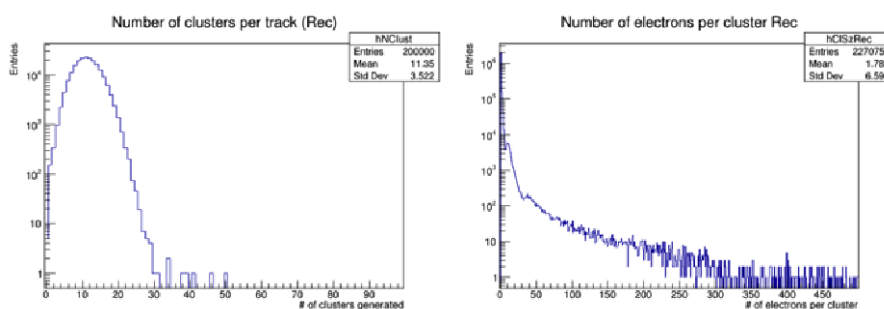


Figure 5.6. Algorithm simulation of a 300 MeV/c muon, 200 hits, 1 cm wide.
Distributions of the number of clusters/cm (left) and of cluster size (right).

The algorithm successfully reproduces the expected distribution of the number of clusters and the cluster size distribution. All algorithms, moreover, have been tested for all particle types over the full momentum range providing consistent results in all cases.

5.4 Geant4 simulation of ionization clustering

At this point, starting from the energy loss distribution calculated by Geant4 - the energy loss is the only necessary information to be provided to the algorithms - and making use of the algorithms derived by the Garfield++ predictions, one can perform, in the framework of Geant4 the same simulation of ionization clustering in a fast and global way avoiding the cumbersome task of following the ionizing particle through the volume of a large detector, as done in Garfield++. Figure 5.7 shows the distributions thus obtained. Except for irrelevant differences in the cluster size distribution, one can conclude that the model derived from Garfield++ and applied to Geant4 provides results, which are in good agreement with the very detailed simulations of Garfield++.



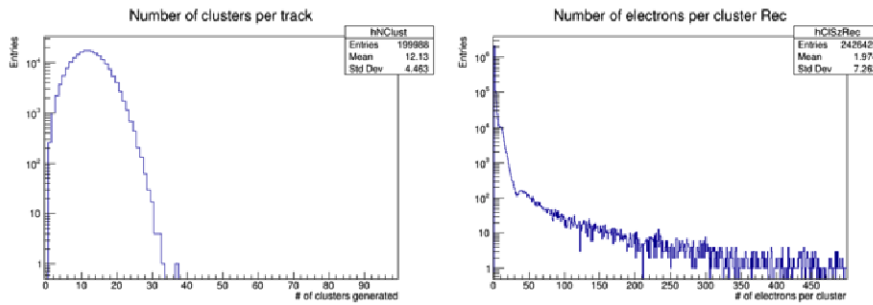


Figure 5.7. Geant4 simulation of a 300 MeV/c muon, 200 hits, 1 cm wide. Distributions of the number of clusters/cm (left) and of cluster size (right).

5.5 Discrepancy between Garfield++ and Geant4 results

Having acquired confidence that the model algorithm derived by Garfield++ and inserted in Geant4 successfully reproduces the distribution of the number of clusters and the cluster size distribution, one can attempt at simulating, under the same conditions, the particle separation, both in dE/dx and in dN/dx , as a function of the momentum for the different particle types in both frameworks, Garfield++ and Geant4.

Figure 5.8 summarizes the results underlining a clear discrepancy. Considering, as an example, the π/K separation at 5 GeV/c momentum, one gets with the dE/dx method a separation of 4.5σ from the Garfield++ simulation as opposed to a separation of only 3.0σ from the Geant4 based simulation. Likewise, with the cluster counting method, one gets 7.5σ and 6.2σ , respectively. The slight differences in the distribution of the number of clusters and the cluster size distribution do not justify such a large discrepancy.

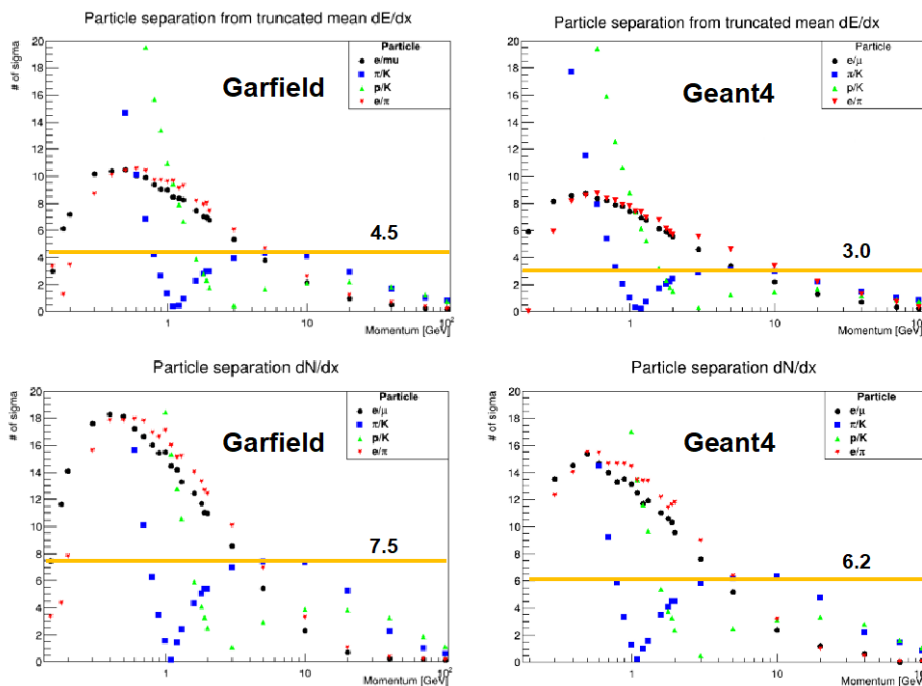


Figure 5.8. Comparison between particle separations as a function of momentum with Garfield++ (at left) and Geant4 (at right) simulations. Top row: separation in terms of dE/dx . Bottom row: separation in terms of dN/dx .



5.6 Motivation for a beam test

The question: “why particle separation, both with dE/dx and with dN/dx , in Geant4 is considerably worse than in Garfield++?” arises. Unfortunately, the lack of experimental data on cluster density and cluster population for He based gas, particularly in the relativistic rise region does not allow for an answer to this question. Moreover, if one looks at Figure 5.9, despite a higher value of the dN/dx Fermi plateau relative to the minimum ionizing value compared to dE/dx , why is the Fermi plateau reached at lower values of $\beta\gamma$ with a steeper slope?

We believe that these questions are crucial for establishing the particle identification performance at SCTF (but also at FCCee, CEPC) and the only way to ascertain these issues is an experimental measurement!

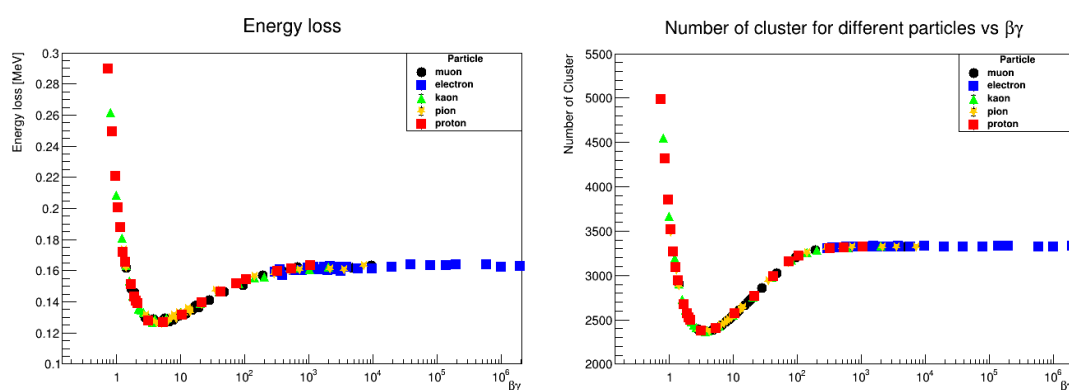


Figure 5.9. Energy loss (left) and total number of clusters for 200 hits, 1 cm wide, tracks of different particle types in 90%He-10%iC₄H₁₀ gas, as a function of $\beta\gamma$.

5.7 The test setup

Besides trying to answer to the above questions, the final goals of the beam test are:

- To ascertain the Poisson nature of the cluster counting technique;
- To establish the most efficient cluster counting and electrons clustering algorithms among the various ones proposed, as a function of the operative parameters like gas mixture, gas gain, geometrical configuration (drift cell size, sense wire diameter, angle between wire direction and ionizing track);
- To define the limiting effects for a fully efficient cluster counting, like the cluster dimensions, the space charge density around the sense wire and the dependence of the counting efficiency versus the impact parameter;
- To demonstrate the ability to count the number of electron clusters released by an ionizing track at a fixed $\beta\gamma$ (e.g., muons at a fixed momentum) as a function of the cell size (1, 2 and 3 cm), of the angle between the track and the normal to the wire direction (from 0° to 60°), of the gas mixture (90% He - 10% iC₄H₁₀ or 80% He - 20% iC₄H₁₀ with, respectively, 12 and 20 clusters/cm for m.i.p.);
- To establish the limiting parameters for an efficient cluster counting, like cluster density as a function of impact parameter, space charge as a function of the gas gain, of the sense wire diameter and of the track angle) and gas gain stability;



Once a set of parameters optimizing the cluster counting efficiency has been defined, a similar experimental setup will undergo a new test in a muon beam of momenta in the relativistic rise range, from minimum ionizing to the Fermi plateau, in order to precisely define the particle identification capabilities of the cluster counting approach over the full range of interest for all future lepton machines.

The current test has been performed during November 2021 at CERN on the H8 beam line in a parasitic mode. Main users on the same beam line were a team testing a tile calorimeter and, therefore, requesting for large part of the time beams of electrons and hadrons, at various energies, needed for their calibration, but useless for our purposes. Only sporadically, a beam of 165 GeV/c muons was available for us.

Figure 5.10 shows schematically the set of 11 drift tubes and their arrangement on the beam line.

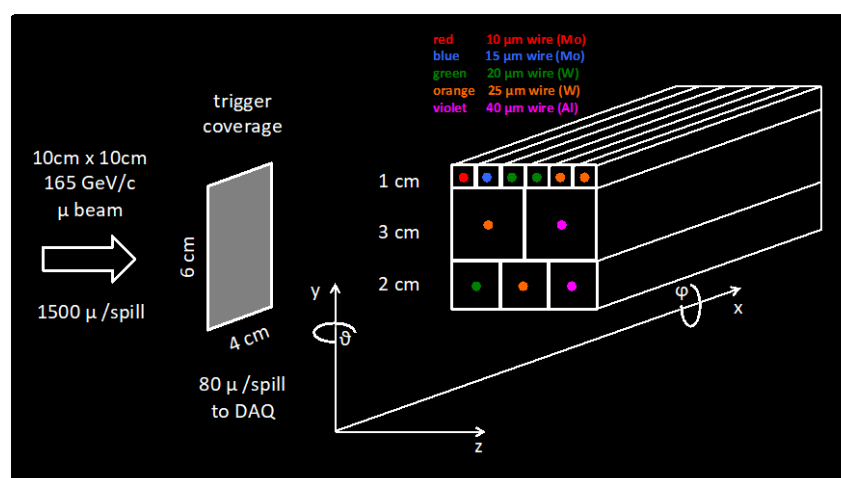


Figure 5.10. The 11 drift tubes (of different size and instrumented with different sense wires, as indicated). Beam intensity, trigger coverage and acquisition rate are shown.

Figure 5.11 is a picture taken from upstream of the beam line and shows all details of the drift tubes (hidden by the copper tape shielding) setup.

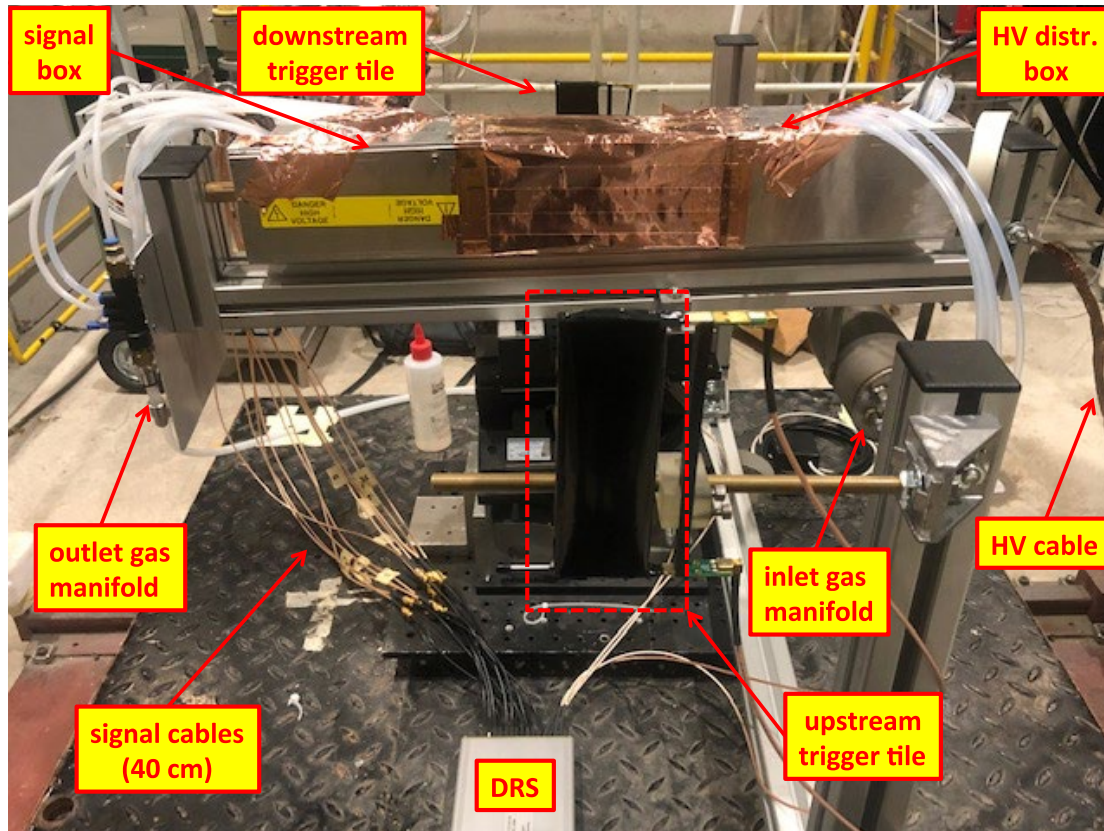


Figure 5.11. The experimental setup seen from the beam upstream. The main components of the setup are indicated by the yellow insets.

The advantages of such a setup are quite a few:

- no need of external trackers: we are only interested in the constant path length inside the drift tube active volume;
- no need of internal tracking (t_0 calibrations, alignment, track finding and fitting algorithms, ...);
- no need to convert time to distance (no time-to-distance conversion, we just count clusters in the time domain);
- no worry of multiple scattering (irrelevant for path length differences at these momenta);
- no need of particle tagging in hadron beams: use only muon beams at different momenta (to explore different $\beta\gamma$);
- use selected commercial amplifiers, neglecting power consumption, to minimize electronics performance limitations and fully integrated digitizers for ease of readout.

The heart of the acquisition system is the Wave Dream Board (WDB), shown in Figure 5.12, developed at PSI for the MEG2 experiment (Ritt S. et al., *Application of the DRS chip for fast waveform digitizing*, *Nucl. Instr. Meth. A*, **623** (1) (2010), pp. 486-488; L. Galli et al., *WaveDAQ: An highly integrated trigger and data acquisition system*, *Nucl. Instr. Meth. A* **936**, 399 (2019)). It contains 16 channels with variable gain amplification and flexible shaping through a programmable pole-zero cancellation.



Two DRS4 chips are connected to two 8-channel ADCs, which are read out by a Field-Programmable Gate Array (FPGA). In normal operation, the DRS4 chips work in “transparent mode”, where they sample the input signals continuously at a speed up to 5 GSPS in an analogue ring buffer. At the same time, a copy of the input signal is sent to the DRS4 output, where it is digitized continuously by the ADCs at 80 MSPS with a resolution of 12 bits. The output stream of the ADCs is used in the FPGA to perform complex trigger algorithms such as a threshold cut on the sum of all input channels. The WDB can be used in stand-alone mode, where it is read out through Gigabit Ethernet. An ultra-low noise bias voltage generator has been implemented in the WDB to power up, through the signal cables, SiPMs.



Figure 5.12. *The Wave Dream Board.*

Figure 5.13 shows the display of one event acquired with the WDB. Its interface acts in analogy to an oscilloscope, as can be seen from the left side of Figure 5.13. The first four channels represent the trigger scintillators (upstream and downstream of the drift tube setup), readout by SiPMs power up by the WDB. The trigger (coincidence of the 4 channels) is generated internally by the WDB. The successive 6 channels are the signal on the row of 1 cm drift tubes, hit by the same beam muon.

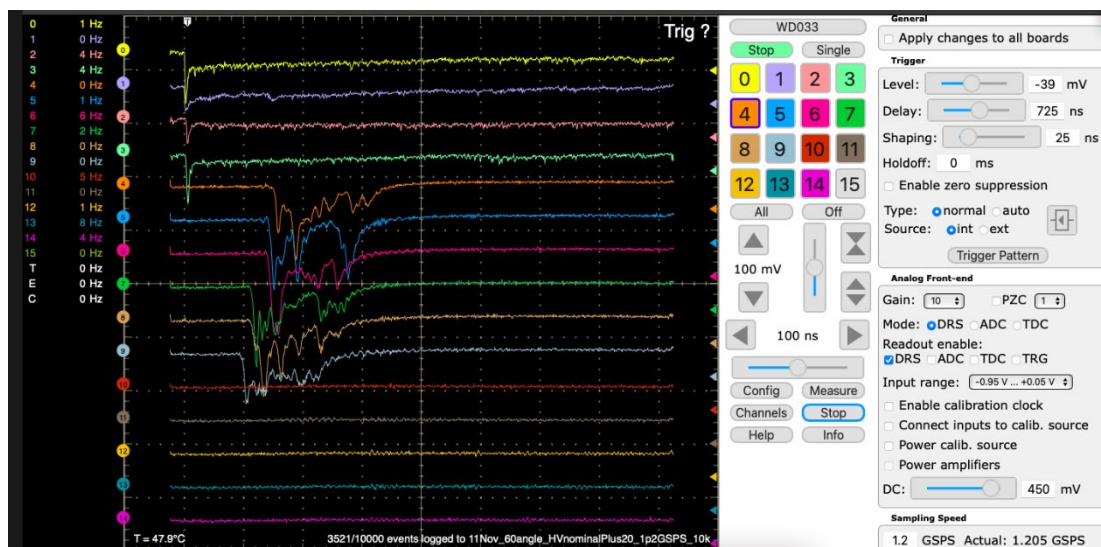


Figure 5.13. The event display of the Wave Dream Board. On the left side, the control panel of the WDB for the channels setup (gain, threshold, bias voltage, etc.) and for accessing the trigger definition panel.

The events, written in binary format, out of the WDB are converted in Root format and shown in Figure 5.14. The first row of four channels represents the trigger scintillator signals in all three plots. In the left plot one can see a muon passing through the row of the 6 drift tubes, 1 cm wide. In the central plot, a muon passing through the row of the 3 drift tubes, 2 cm wide. In the right plot, a muon passing through the row of the 2 drift tubes, 3 cm wide. The full vertical scale is 300 mV and the horizontal scale is 900 ns. All channels are amplified by a factor 10.

To be noticed is the very favorable ratio of signal to noise and the clean evidence of the structure of the signal in clusters.

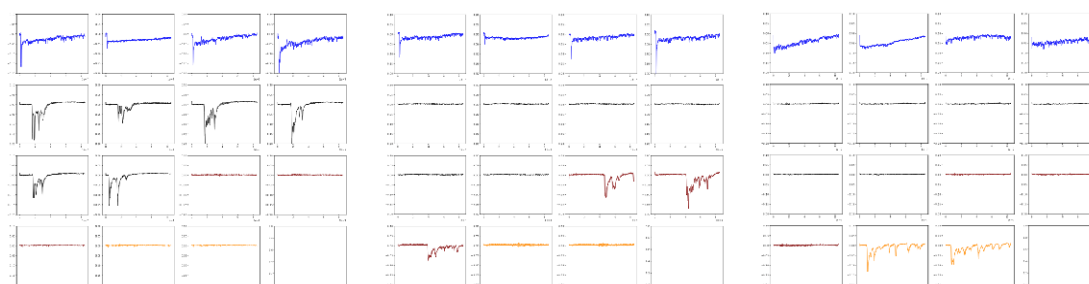


Figure 5.14. Three events converted in Root format. The first row of four channels represents the trigger scintillator signals in all three events. In the left plot, a muon crossing the row of the 6 drift tubes, 1 cm wide. In the central plot, a muon crossing the row of the 3 drift tubes, 2 cm wide. In the right plot, a muon crossing the row of the 2 drift tubes, 3 cm wide. Scale is 300 mV vertical and 900 ns horizontal. All channels are amplified by a factor 10.

5.8 Preliminary results on gas gain

The gas gain at a given anode voltage has been calculated by fitting with a Landau function the average single electron pulse height (Figure 5.15) and correcting the obtained most probable value for the amplifier gain, for the impedance mismatch between the characteristic tube impedance and the 330 Ω termination resistor on all tubes and for the current divider between the 330 Ω termination resistor and the 50 Ω input impedance of the ADC.

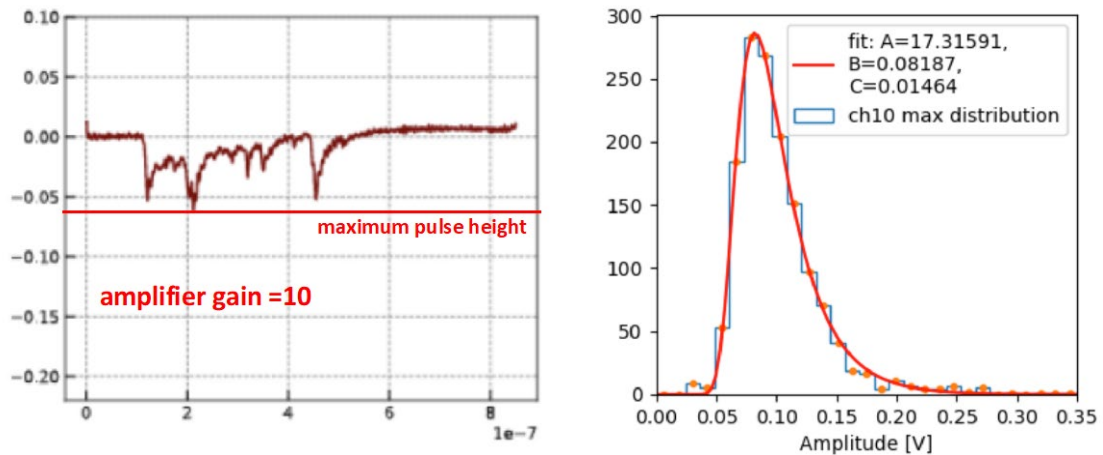


Figure 5.15. A right, the Landau fit to the distribution of the maximum pulse height (left plot). The MPV value is then used for the calculation of the gas gain.

In Figure 5.16 the gas gain is plotted as a function of the anode high voltage for drift tubes configurations, for the 90% He - 10% iC_4H_{10} gas mixture and for a pressure of 725 torr.

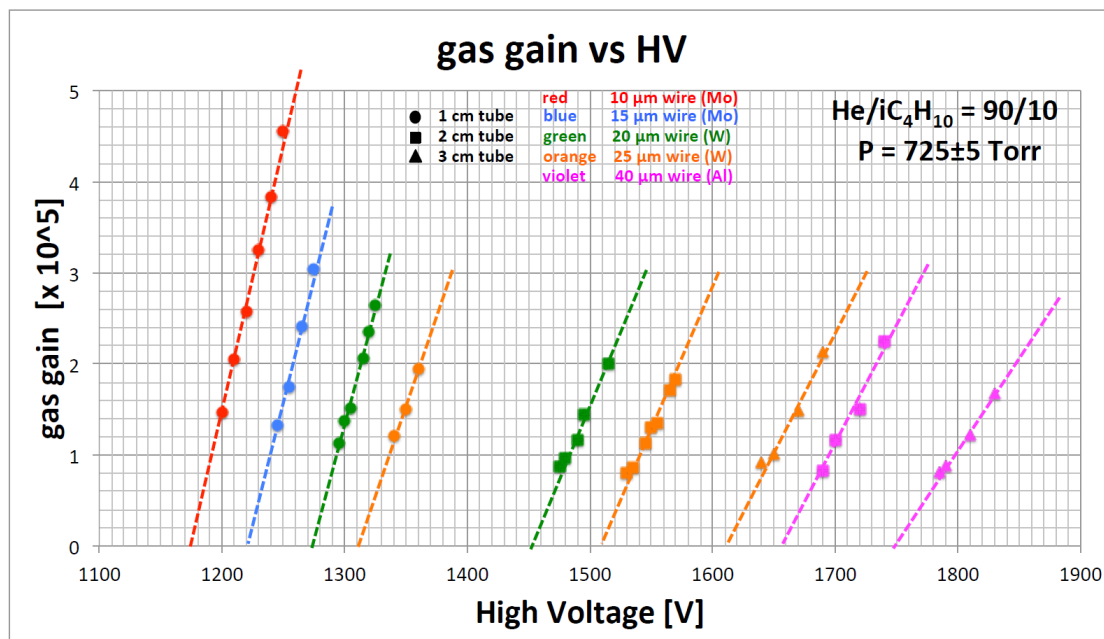


Figure 5.16. Gas gain as function of the anode high voltage for the different configurations of the tested drift tube. The gas mixture and the gas operating pressure are indicated in the figure.

5.9 Preliminary results on space charge

We have studied the single electron avalanches overlap as a function of the angle α between the track direction and the normal to the sense wire (Figure 5.17).

Space charge effect, at any given angle, results in reducing the effective gas gain (or, equivalently, the average single electron pulse height) with respect to a configuration at a larger angle. At 165 GeV/c and 90% He - 10% iC_4H_{10} gas mixture, we expect the number of cluster to be $N \sim 16.5/cm$ with, therefore, an average separation λ between consecutive

clusters along the track of the order of 600 μm . Figure 5.17 shows the avalanche separation, $\lambda \sin\alpha$, projected on the sense wire.

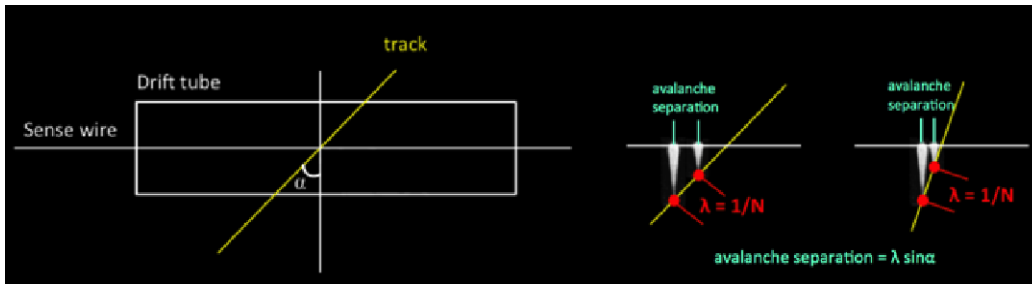


Figure 5.17. Space charge effects depend on the angle α between the track direction and the normal to sense wire orientation. The avalanche separation projected on the sense wire, $\lambda \sin\alpha$, is indicated.

Figure 5.18 shows at left a plot of the average single electron pulse height as a function of the avalanche separation $\lambda \sin\alpha$ for different gas gains on the 2 cm drift tube instrumented with the 20 μm sense wire. The plot suggests no dependence of space charge effects from the gas gain, at least in this range of gas gain values. Likewise, Figure 5.18 at right, showing the plot of the average single electron pulse height as a function of the avalanche separation $\lambda \sin\alpha$ for different sense wire diameters at approximately equal gas gains for the 1 cm drift tubes, suggests no dependence of space charge effects from the sense wire diameter, at least in this range of gas gain values.

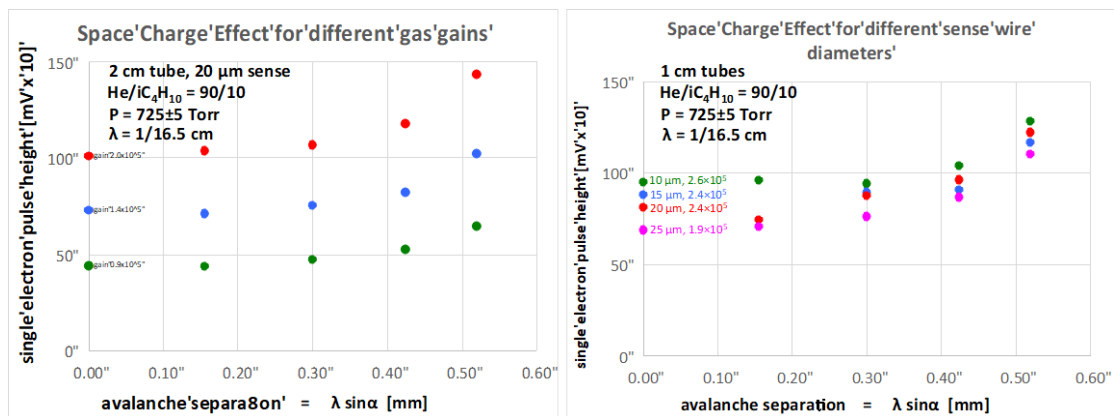


Figure 5.18. Left: Single electron pulse height as a function of the projected avalanche separation for different gas gains in the 2 cm drift tube instrumented with a 20 μm sense wire. Right: Single electron pulse height as a function of the projected avalanche separation for different sense wire diameters at approximately equal gas gain in the 1 cm drift tube.

The space charge effect for this gas mixture, results in approximately 70% maximum avalanche suppression, at $\alpha=0^\circ$.

A naive model based on spherical shape of the avalanche gives, for these particular configurations, an avalanche radius r_{av} of approximately 450 μm .

The condition of no avalanche overlap: $\lambda \sin\alpha \geq 2 r_{av}$, in this case, is met for $1/\lambda = N \geq 11/\text{cm}$. Any helium/isobutane gas mixture richer than 10% isobutane (corresponding to $N = 12/\text{cm}$ at m.i.p.) will, therefore, necessitates space charge effects corrections for an efficient application of the cluster counting techniques.



5.10 Preliminary results on cluster counting algorithms

We have started to use different cluster counting algorithms to analyze the collected data. We are following four different approaches for isolating the electron peaks in the signal spectra: the Beijing algorithm, the Lecce algorithm, the Louvain algorithm, and the Novosibirsk algorithm. Direct comparisons among the different algorithms are very valuable for improving the overall individual counting efficiencies.

The Beijing algorithm is based on a moving average smoothing and first and second derivative analysis of the signal spectra. The association of electrons in clusters is very preliminary and still needs some refinement.

The Lecce algorithm is analogous to the Beijing one. The association of electrons in clusters is based on the different distributions of the relative delays of consecutive electron peaks belonging to the same cluster with respect to those belonging to separate clusters. This criterion has proved very strong in simulations, and we are currently working to optimizing it for the data collected.

The Louvain algorithm uses two different approaches. The first one uses a very promising continuous wavelet transform (CWT) tool, which, however, still needs to be optimized. The second one is based on the Savitzky-Golay filter to smooth out the noise and on second derivative for peak finding. No association of electrons to clusters has been tried yet.

The Novosibirsk algorithm is based on the dynamic estimation of the baseline level defining a sequence of local minimum - local maximum - local minimum as a peak accounting for the baseline shifts caused by the previous found peaks. It uses the peak clusterization algorithm described in section 6.4.2. Its efficiency will soon be improved from the actual low value of 50%.

Figure 5.19 shows the same signal analyzed by four different algorithms with marks around the found peaks. These are just first attempts and no effort has been placed in the optimization of the various peak finding parameters. However, even with large inefficiencies, the direct comparison among the different algorithms represents a powerful tool for improving the peak finding efficiency and reducing the fake peak rate.



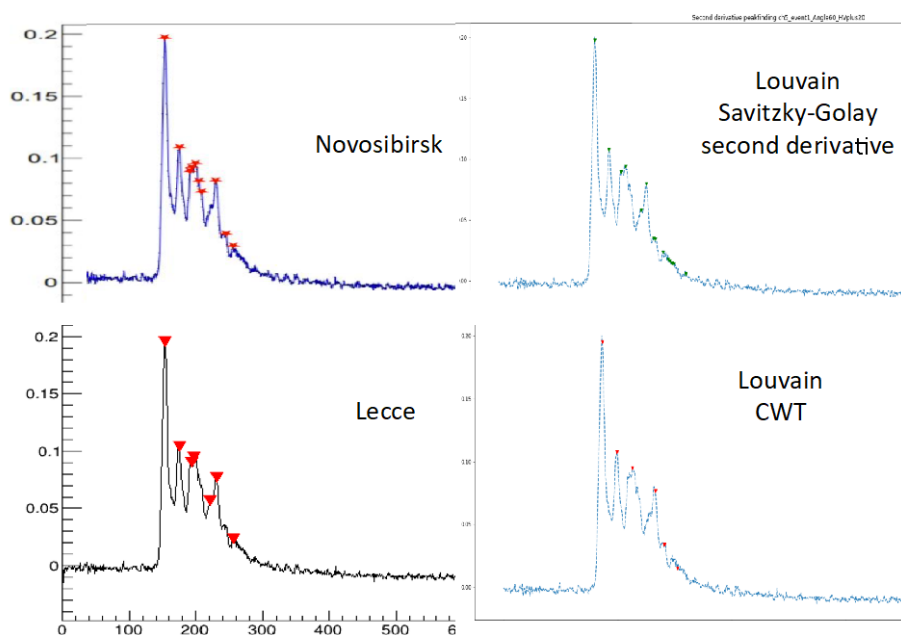


Figure 5.19. The same signal analyzed with very preliminary versions of different algorithms, as indicated in the insets. The direct comparison among the various algorithms is of great help in improving the peak finding efficiency and reducing the fake peak rate.

6. Simulation of the SCTF drift chamber

The main stages of the simulation of events in the SCTF drift chamber (DC) are the following:

- generation of the DC geometry;
- Simulation of the particles passage through the DC material;
- Simulation of the digitized signals from the wires;
- Hits reconstruction;
- Track finding;
- Track fitting;
- Particle identification.

Below we give a brief description of the current state of affairs for each item.

6.1 Generation of the DC geometry

As a basic option for SCTF detector the full-stereo DC with square cells is considered, see Figure 6.1. The layers of cells are grouped into 8 super-layers with 8 layers each. The chamber volume is filled with a 90% He - 10% iC_4H_{10} gas mixture. The amount of material traversed by a particle flying in a straight line with polar angle $\pi/2$ is $3.8 \times 10^{-4} X_0$ for the gas and, on average, $10.0 \times 10^{-4} X_0$ and $7.8 \times 10^{-4} X_0$ for signal and field wires, respectively.

The major DC geometry parameters used in our simulation are listed in Table 6.1.



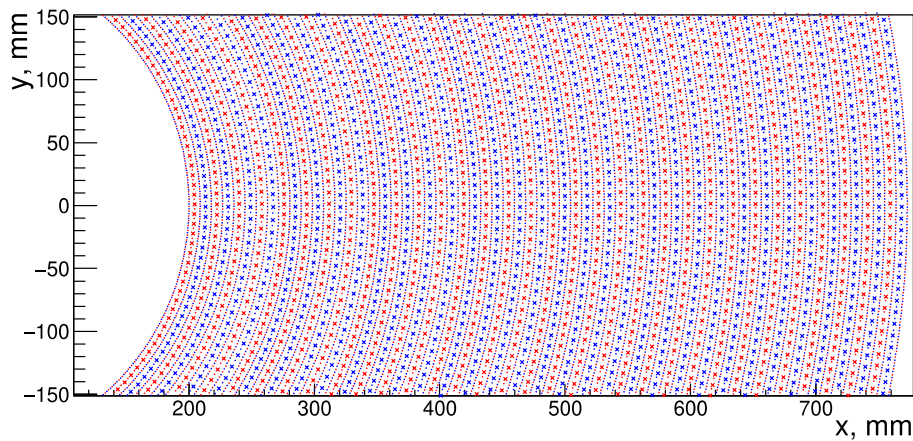


Figure 6.1. Signal (crosses) and field (dots) DC wires at $z=0$. Red and blue colors correspond to the stereo angle sign.

Table 6.1 Configurable (upper part of the table) and derivable (lower part) parameters of the DC geometry.

Parameter	Value
Inner radius R_{in}	200 mm
Outer radius R_{out}	800 mm
Length L	1800 mm
Azimuthal angle between wire ends α	$\pi/6$ rad
Number of superlayers $N_{superlayers}$	8
Number of layers in superlayer N_{layers}	8
Diameter and material of signal wire	25 μm , W
Diameter and material of field wire	50 μm , Al
Cell dimension	$\approx 7-9$ mm
Stereoangle ϵ	$\approx 60-220$ mrad
Total number of signal wires $N_{signal\ wires}$	21824
Total number of field wires $N_{field\ wires}$	109780

To simulate the passage of particles through the detector material the DC geometry is transferred to GEANT4 package (*GEANT4 Collaboration (Agostinelli, S. et al.). GEANT4: A Simulation toolkit. Nucl.Instrum.Meth. A506 250-303 SLAC-PUB-9350, FERMILAB-PUB-03-339, 2003*) using the DD4HEP toolkit (*Frank, Markus et al. DD4hep: A Detector Description Toolkit for High Energy Physics Experiments*).

6.2 Simulation of the particles passage through the DC material

All the data necessary for simulation of the creation and drift of ionization in the DC gas volume and for the simulation of avalanche amplification were obtained with the Garfield++ package (*H. Schnidler. Garfield++ User Guide. User Manual, 2021.1, 2020*).

The output of GEANT4 simulation is a collection of tracking steps for the particles in the DC gas. For each of these steps we generate the positions of the ionization clusters according to their average number per unit length $dN_{cl}/dx(\beta\gamma)$ at the given particle velocity β (Figure 6.2). Furthermore, according to the energy transfer spectrum in the ionization act (Figure 6.3) we generate the cluster energy and the number of electrons it comprises.



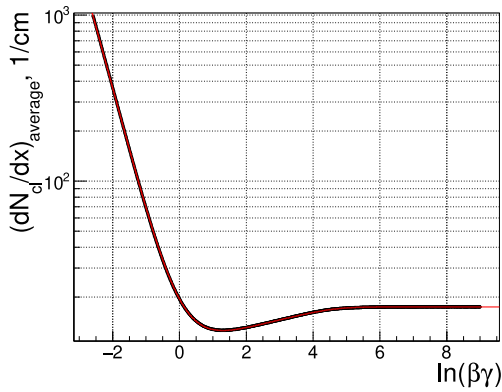


Figure 6.2. The dependence of average dN_{cl}/dx on $\beta\gamma$ according to Garfield++ (black markers) and its approximation (red curve).

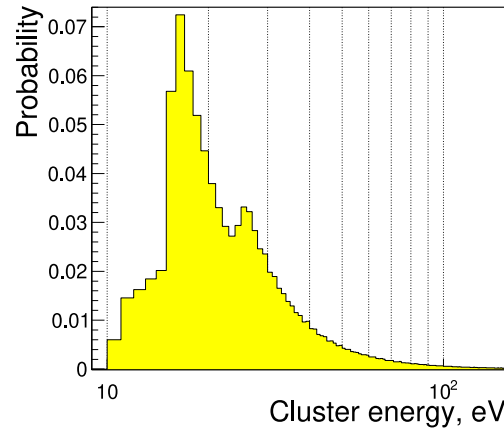


Figure 6.3. Cluster energy spectrum for the particles with velocity $\beta=0.99$.

6.3 Simulation of the digitized signals from the wires

To calculate the drift time of the ionization electrons we use the isochrones map, shown in Figure 6.4, obtained with Garfield++ in the approximation of the axial wires. For each electron the avalanche amplification factor is generated according to the spectrum, shown in Figure 6.5 and the induced signals at two wire ends are scaled using the charge division formula (CDF).

Next, the shaped signals from both wire ends are digitized with 2 GHz sampling rate. Since it is too resource prone to save the whole digitized waveform, we developed an ad-hoc peak finding algorithm to find the times and the amplitudes of the peaks corresponding to the individual avalanches.

The idea of the algorithm is to consider each local maximum in the waveform as a possible peak and to estimate the statistical significance of its deviation from the current baseline level. The estimation of the baseline is based on the amplitudes of three preceding peaks and on the knowledge of the signal shape decay rate. Figure 6.6 shows the example of found peaks in the waveform for muon.

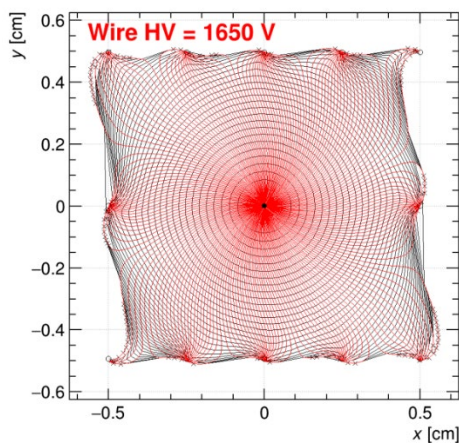


Figure 6.4. Isochrones (black curves) and drift lines (red curves), obtained from Garfield++ for axial

squared cells 10×10 mm². Signal wires Voltage is 1650 V, the magnetic field $B = 1$ T.

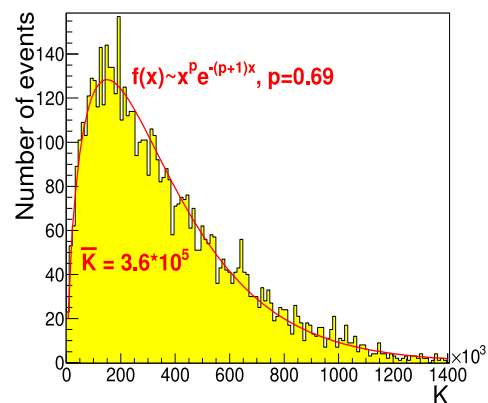


Figure 6.5. Spectra of the avalanche amplification and its approximation by the Polya distribution

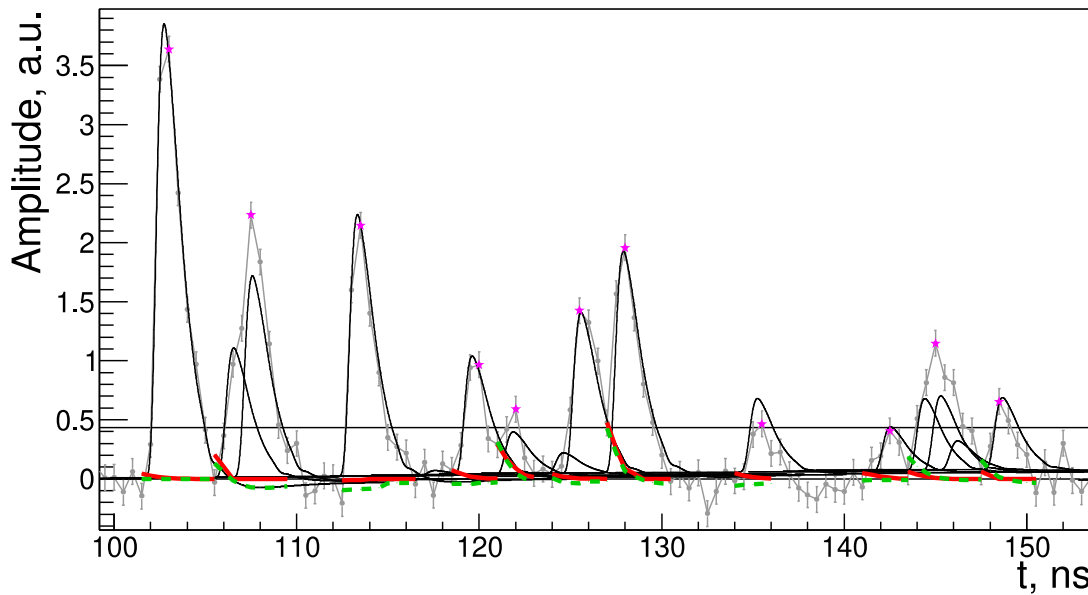


Figure 6.6. The peaks (magenta markers) found in the digitized wire waveform (gray graph) for μ^+ . Black curves show the signals from the avalanches, red and green graphs the calculated and truth baseline, correspondingly.

6.4 Hit reconstruction

6.4.1. Peaks merging and z-coordinate reconstruction

The digitized wire hit contains the sets of times and amplitudes of peaks found in the signals from both wire ends. Using each of these sets we reconstruct (with some accuracy) the original analog signals from the avalanches and determine the arrival time difference t_{shift} between them via the maximization of their cross-correlation. Then, after the time alignment of these analog signals, we merge the pairs of peaks having the largest overlap, see Figure 6.7, and discard the remaining unpaired peaks as noise.

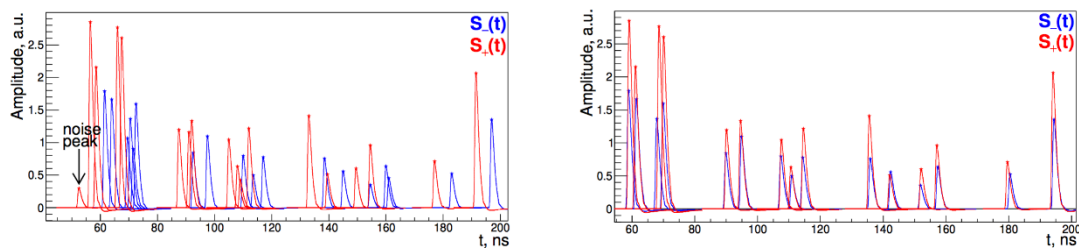


Figure 6.7. Reconstructed analog signals from both wire's ends before (left) and after (right) merging of peaks.

Notice that the value of t_{shift} allows the hit's z-coordinate reconstruction with an accuracy of $\sigma_z \approx 20$ mm, which is few times better than the accuracy of CDF-based reconstruction, see Figure 6.8.

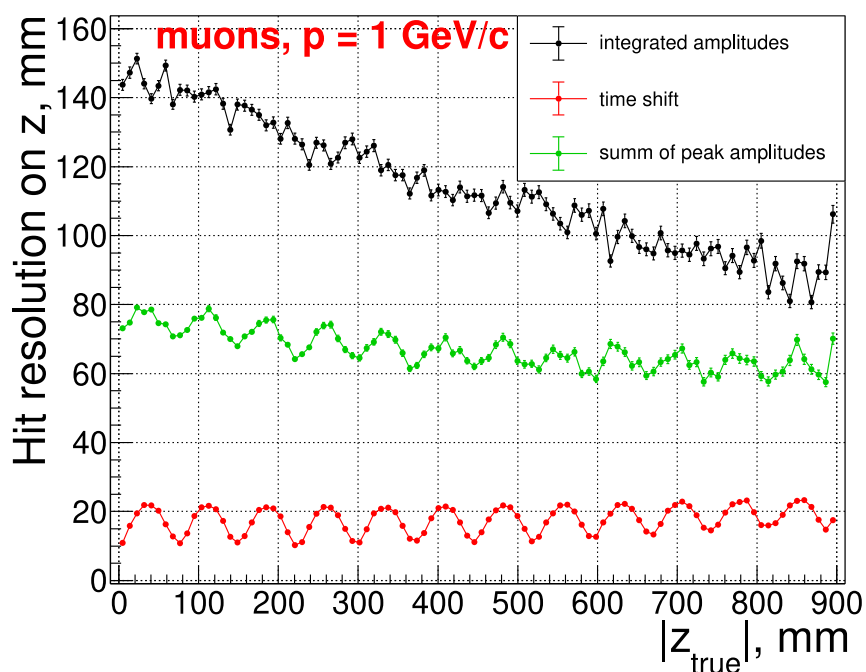


Figure 6.8. Resolution on z -coordinate, reconstructed via the t_{shift} (red graph) and via the CDF using the full integrated amplitudes (black graph) and sums of the peak amplitudes (green graph) depending on the truth z -coordinate for the μ^+ with 1 GeV/c momentum.

6.4.2. Peaks clusterization

An ionization cluster with more than one electron typically produces more than one peak in the waveform, therefore the task of cluster counting requires the development of efficient peaks clusterization algorithm (CA). The main sources of clusterization inefficiency are:

- The overlap of the (sets of) peaks from different clusters;
- The loss of peaks with low amplitude;
- The absorption of electrons during the drift.

We developed the CA based on the description of set of merged peaks by a gaussian mixture model, where each gaussian corresponds to an individual cluster. The positions of gaussians are determined using the Expectation Maximization algorithm.

The goal of CA is to determine the number and positions of clusters, for which the optimum is achieved between the likelihood of data description and the model complexity (i.e. the number of clusters). We use the Akaike information criterion to find this optimum. Figure 6.9 shows an example of operation of the described CA. Notice that our current CA version is very preliminary and has a very low cluster reconstruction efficiency (approximately 50%) even for minimum ionizing particles, and we are working to improve it.



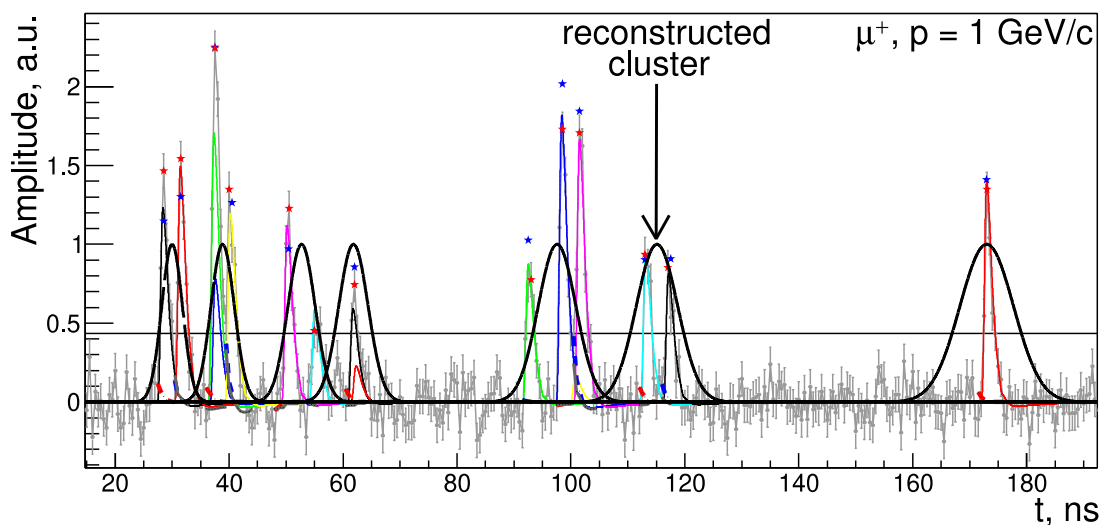


Figure 6.9. The reconstructed clusters (black gaussians) in the waveform for the μ^+ with 1 GeV/c momentum.

6.4.3. Reconstruction of track impact parameter

In the existing drift chambers, the distance to the "first cluster" $\rho_{f.c.}$ is used to estimate the track impact parameter ρ_{PCA} relative to the wire. However, the discreteness of ionization makes this estimation systematically biased. The reconstruction of clusters in the SCTF DC allows one to reduce this bias significantly with help of the Maximum Product of Spacings (MPS) algorithm (*G. Signorelli, A. D'Onofrio, and M. Venturini. A novel method to estimate the impact parameter on a drift cell by using the information of single ionization clusters. Nuclear Instruments and Methods in Physics Research Section A 824:581–583, 2016.*). The idea of the latter is to find the impact parameter ρ_{MPS} , for which the sample of cluster positions along the track corresponds maximally to the uniform distribution, see Figure 6.10.

The MPS algorithm was implemented in our simulation and the performed test confirmed the expected bias reduction, see Figure 6.11.

6.5 Track finding

The reconstruction of events in the DC starts from the procedure of track finding (TF). As the TF algorithm, suitable for the full-stereo SCTF DC, we chose, initially, a local track following algorithm. Up to the moment we have implemented only the initial steps of this algorithm, namely the reconstruction of hit doublets (pairs of intersecting triggered wires in consecutive layers) and of the chains of doublets, i.e. the initial track segments, used as the starting points for the track following (extrapolation), see Figure 6.12.

6.6 Track fitting

The approximation of tracks in the SCTF DC is performed in two stages:

- preliminary Riemann fit (*A. Strandlie et al. Treatment of multiple scattering with the generalized Riemann sphere track fit. Nuclear Instruments and Methods in Physics Research A, 2002; A. Strandlie et al. Exploration and extension of an improved Riemann track fitting algorithm. Nuclear Instruments and Methods in Physics Research Section A 867 2017.*)



- final fit with Kalman filter (*Johannes Rauch and Tobias Schluter. GENFIT – a Generic Track-Fitting Toolkit. J. Phys. Conf. Ser., 608(1):012042, 2015.*) using the results of Riemann fit as an initial approximation.

The preliminary estimation of the momentum and angular resolutions of tracks are shown in Figure 6.13. It can be seen that the usage of MPS-algorithm leads to 10-15% improvement in the DC resolutions compared to the usual "first cluster" approach. However, we underline again the preliminary nature of the above estimations, since:

- currently, we use the approximation of circular isochrones in the time-to-distance relations, which is a very rough approximation;
- the MPS algorithm crucially depends on the efficiency of peaks clusterization algorithm, which is preliminary very low.

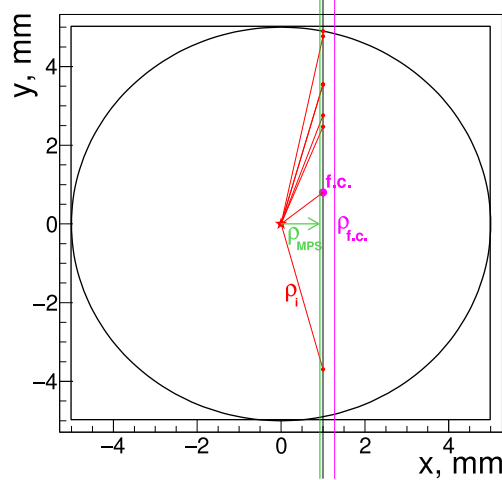


Figure 6.10. Particle track (black line) and ionization cluster (red markers). Magenta and green lines show the reconstructed tracks with impact parameters $\rho_{f.c.}$ and ρ_{MPS} .

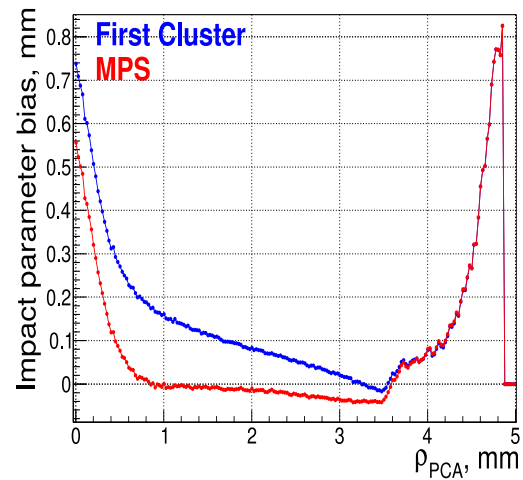


Figure 6.11. The bias of the impact parameter $\rho_{f.c.}$ or ρ_{MPS} depending on ρ_{PCA} in the simulation of μ^+ with 1 GeV/c momentum.

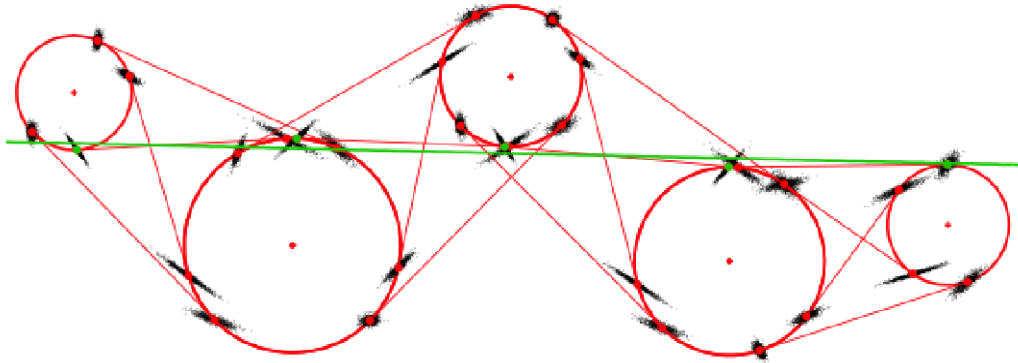


Figure 6.12. The chain of four wire doublets. The red markers show the tangent points of the lines, the "clouds" of the black points show the uncertainties of the position of the tangent points. Green markers show the tangent points, corresponding to the path with the smallest X^2 of the linear fit (green line).

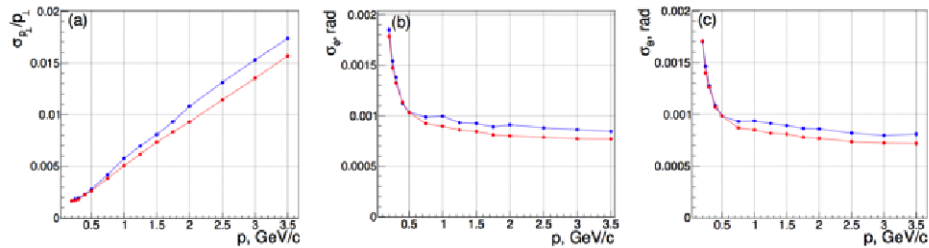


Figure 6.13. Preliminary estimation of the SCTF DC resolutions: (a) resolution on the transverse momentum p_t ; (b) and (c) resolutions on the φ and ϑ angles, respectively. Blue and red curves refer to the use of $\rho_{f.c.}$ and ρ_{MPS} , respectively

6.7 Particle identification

We study the potential of SCTF DC in the particle identification (PID) using the following identification variables:

- specific energy losses dE/dx , calculated via the "truncated mean", i.e., by discarding of 30% ($\eta=0.3$) of drift cells with highest dE/dx ;
- dN_{peaks}/dx with $\eta=0.9$, where dN_{peaks} is the number of merged peaks in the given cell;
- $dN_{cl,MCTruth}/dx$ with $\eta=0.9$, where $dN_{cl,MCTruth}$ is the true number of clusters in the drift cell, known only in simulation. This variable is used for estimation of the theoretical limit of PID efficiency;
- $dN_{cl,reco}/dx$ with $\eta=1.0$, where $dN_{cl,reco}$ is the reconstructed number of clusters in the drift cell.

We calculate the separation power of the pair of particle types via the formula

$$S_{sig/bkg} = |\mu_{sig} - \mu_{bkg}| / [(\sigma_{si} + \sigma_{bkg})/2],$$

where μ is the most probable value of identification variable, $\sigma = FWHM/\sqrt{[2\ln(2)]}$ is the width of its distribution. Figure 6.14 shows the momentum dependences of the separation powers for different pairs of particle types and the identification variables, introduced above. It is seen that the separation power with $dN_{cl,MCTruth}/dx$ (theoretical limit) is about 1.5-2 times larger than that for dE/dx . At the same time, the low efficiency of current version of the clusterization algorithm makes the separation power for $dN_{cl,reco}/dx$ even lower than for dE/dx , and we expect to overcome this

problem in future. Finally, Figure 6.15 shows a comparison of separation powers for different pairs of particle types using the dE/dx and $dN_{cl,MCTruth}/dx$ variables.

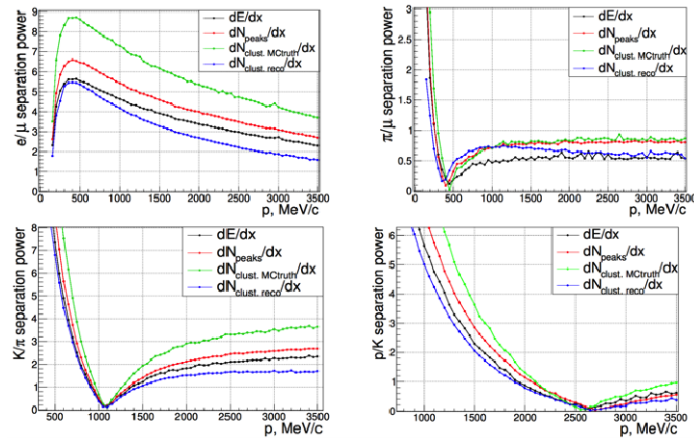


Figure 6.14. The dependencies of e/μ (upper left), π/μ (upper right), K/π (lower left) and p/K (lower right) separation powers on the momentum for different identification variables.

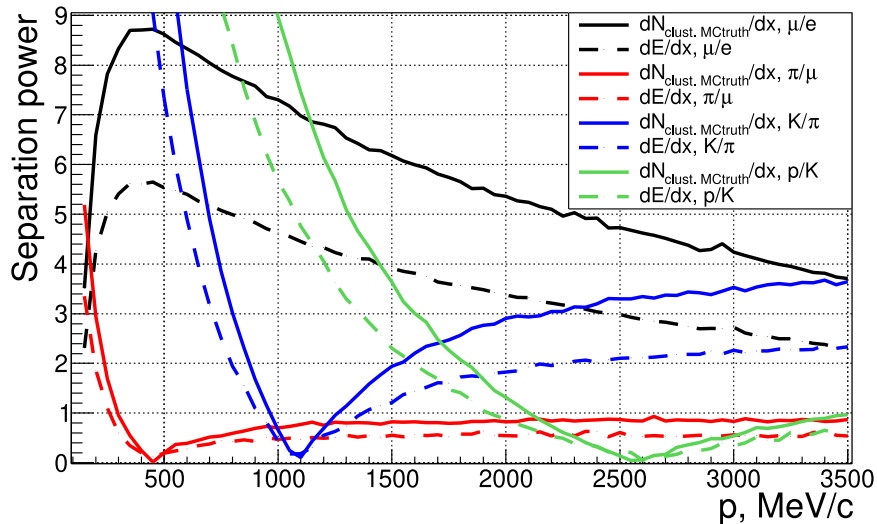


Figure 6.15. The e/μ , π/μ , K/π and p/K separation powers for dE/dx and $dN_{cl,MCTruth}/dx$ variables depending on the momentum.

7. Prospects and conclusions

- **The mechanics of the SCT drift chamber prototype (CMD-3)**

We are going to hire, with Cremlin+ funds, in the next months and for one year, a computational mechanics engineer to complete the FEA calculations for the definition of the optimal configuration of the CMD-3 drift chamber structure, in terms of reducing as much as possible the impact of its transparency versus the crystal electromagnetic calorimeter and, at the same time, preserving its stability.

As soon as this phase is concluded, we intend to build a real scale mockup of one end plate to verify the wire tension recovery scheme and its applicability to the end plates of the SCTF drift chamber TraPId, the design of which will have to be completed by the end of the Cremlin+ project.

- **The BINP Magnetron for wire coating**

The introduction of new replaceable coated cathodes has allowed for a relatively cheaper consumption of the precious sputtered material, while maintaining high-quality thermal contact with the cooled surface of the magnetron, thus reducing the heating of the coated wire. It is also planned to reduce the consumption by 3-4 times by scaling the magnetron.

40 and 50 μm uncoated aluminum wires have been supplied to the BINP team for continuing magnetron coating tests with silver and gold and the delivery of a batch of 36 μm carbon monofilaments, which, at the moment, represents one of the most promising innovations for drift chambers, is expected any time now. The contribution to the radiation length of the active volume of TraPId due to the metallic wires amounts, indeed, to more than 80% of the total (less than 20% is the contribution due to the gas) and could be reduced by a factor 4 with the introduction of carbon wires.

- **Development of a fast digitizer-FPGA board for cluster counting**

With the acquisition of new and more sophisticated hardware, to treat simultaneously two channels and to prove the feasibility of correlating contiguous hits and the improvement of the described CluTim algorithm, both in terms of counting efficiency (currently at approximately 80% level) and in terms of fake rate contaminations (at level of 1-2%), the first phase of this task will be concluded within this year 2022.

The successive step is to develop a 4-channel system and include the hits correlating algorithms to define track segments within the maximum drift time. To this purpose, collaboration with CAEN has been established within a joint project funded by the AIDAInnova program.

- **The beam test for cluster counting**

The analysis of the data collected last November will continue for large part of this year. The cluster counting algorithms need to be optimized and their efficiency must be maximized under the various conditions.

Once a set of optimal parameters has been defined, a similar experimental setup will undergo a new test in a muon beam of momenta in the relativistic rise range, from minimum ionizing to the Fermi plateau, in order to precisely define the particle identification capabilities of the cluster counting approach over the full range of interest for all future lepton machines.

A beam request to CERN has already been placed, for a test period at the beginning of next summer.

- **Simulation and reconstruction in the SCT drift chamber**



The simulation and reconstruction package of TraPId is in a very advanced stage, however, some aspects need to be worked on for the completion of the task.

The first one concerns the clusterization algorithm, which results in a very low cluster reconstruction efficiency (approximately 50%), even for minimum ionizing particles. Besides particle identification, this aspect is particularly relevant for the correction to the impact parameter bias with the described MPS algorithm and affects the improvements in the track parameter resolutions.

A second aspect concerns the track finding task, which is based on the very rough approximation of circular isochrones in the time-to-distance relations. Moreover, the track finding algorithm, suitable for the full-stereo SCTF drift chamber has only been implemented at its initial steps and need to be completed.

